perties of (infinite) periodic crystals. However a surface (both free and internal, such as grain boundary or a stacking fault) can also be treated by this method. In order to do so one constructs a supercell containing elements of structure simulating the surface of interest. In the case of a free surface, one can include layers of empty spheres simulating the vacuum. Fig. 1 schematically illustrates such a cell.

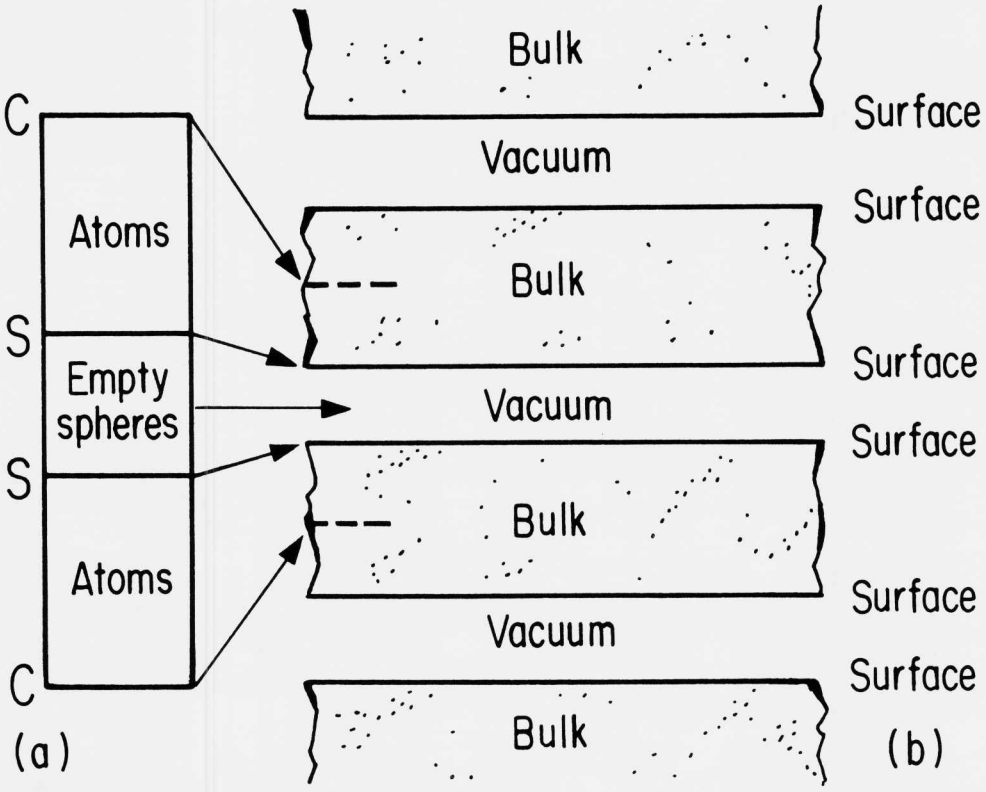

Figure 1. Simulation of surfaces in supercell approach a) Supercell; b) The corresponding infinite array of slabs.

The supercell should be as symmetric as possible in order to reduce the size of irreducible wedge of the corresponding Brillouin zone. The infinite crystal, built of the thus constructed supercells consists of slabs of atoms separated by "cushions" of vacuum (Fig. 1.) To simulate the (100) surface of BCC iron, we have constructed 3 tetragonal supercells, each containing 16 atoms. These are shown in Fig. 2.

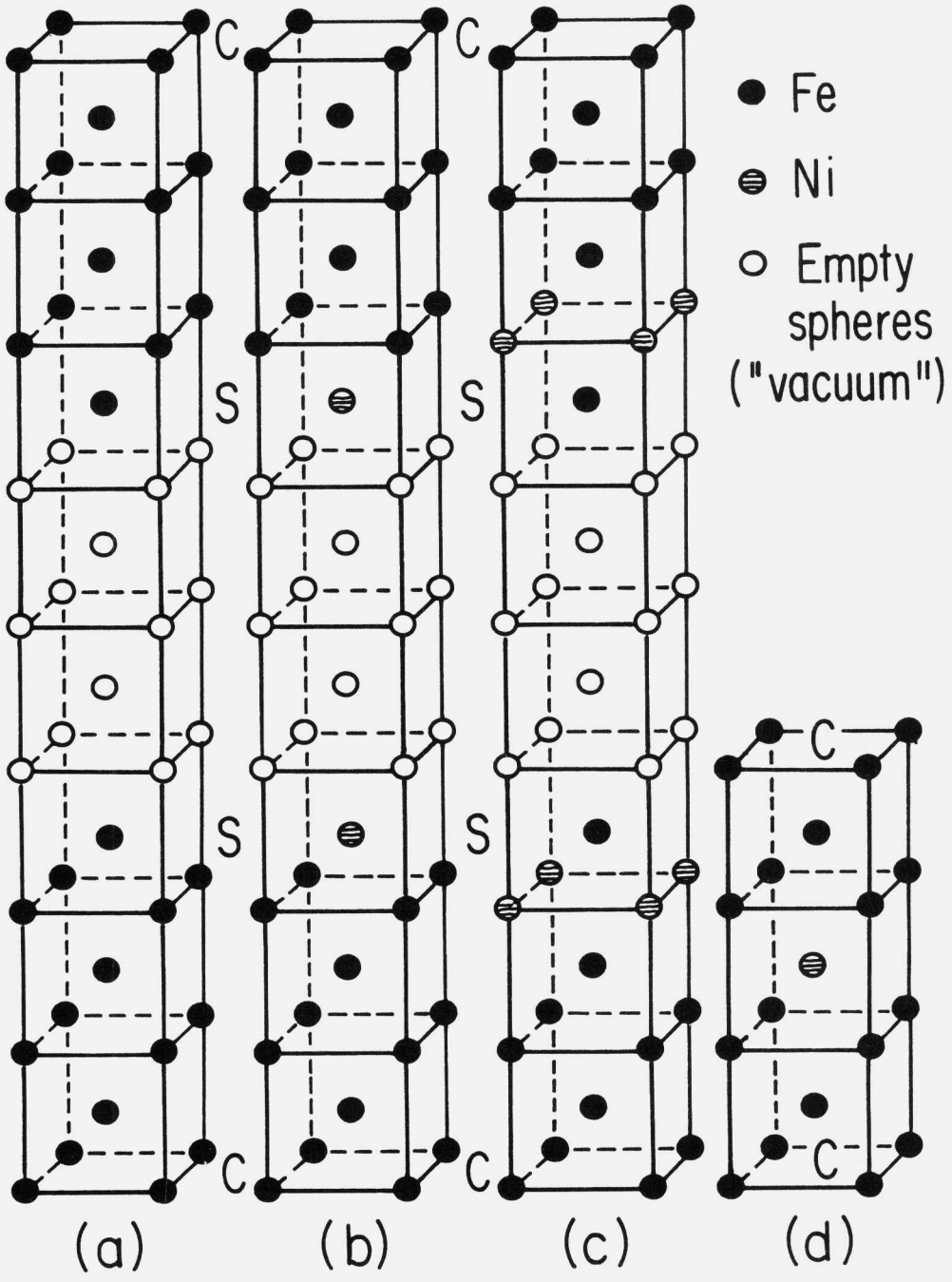

Figure 2. 16 atom supercells; a) pure Fe; b) layer of Ni atoms on the surface; c) Layer of Ni atoms below the surface; S-"surfaces", C-central layers; d) The reference 6-atom supercell.

The pure iron surface is represented by supercell (a). It contains 11 Fe-atoms and 5 empty spheres. If translated along the x, y, and z axis, an infinite system is generated consisting of infinitely wide (in -x and -y directions) slabs of 11 layers of Fe-atoms, separated by vacuum (5 layers of empty spheres). The size of the supercell has been chosen so that the central layer of Fe-atoms (C) would be far enough from the two surfaces (S) in order to be almost "bulk"-like. On the other hand, the thickness of the vacuum cushions should be sufficient for the two adjacent surfaces not to significantly interact.

In supercell (b) the surface layers of Fe atoms are replaced by Ni-atoms; both the dimensions and the overall number of spheres of supercell (a) are preserved. In supercell (c) we substitute the layer of Fe right below the surface with Ni.

According to thermodynamic definition, the surface energy γ can be expressed as:

$$\gamma = \frac{E_{\text{supercell}} - E_{\text{reference}}}{2\sigma} \qquad (1)$$

where $E^{\text{reference}}$ is the energy of the same atoms in the bulk environment; σ is the surface area per atom and the factor 2 in the denominator appears because the super cell contains two surfaces.

In the case of the pure iron surface (a), the reference system is simply eleven iron atoms in bcc coordination, i.e.

$$E^{\text{reference}} = 11E^{Fe,BCC}$$

In cases (b) and (c) the reference system has to contain two isolated layers of Ni atoms in bulk of iron. In order to simulate such a system, we constructed a reference 6 atom supercell consisting of one Ni and 5 Fe atoms (Fig. 2(d)). Then $E^{\text{reference}}$ in Eq.(1) can be approximated as:

$$E^{\text{reference}} = 2E^{Fe_5Ni} - 1E^{Fe,bcc}$$

The results of our calculations are presented in the next section.

4. RESULTS

Bond-Counting Model

Before discussing the results of the supercell calculations it is worthwhile to mention a simple empirical method of estimating the surface energy (see, e.g. [31]) The method is based on counting the number of broken bonds when an atom is removed from the bulk onto the surface, using the regular solution model. In the case of a pure component A, the surface energy, γ_A is simply:

$$\gamma_A = - \frac{Z^v \varepsilon^{AA}}{2\sigma} \tag{2}$$

where Z^v is the number of vertical bonds made by the atom to each of the adjacent atom layers, and ε^{AA} is the A-A interaction energy. In Eq. (2) only the nearest neighbors are taken into account.

Making use of the same supercells (a)-(d) and the definition of the surface energy, Eq. (1), more general expressions allowing for interatomic interactions within two shells of neighbors can be written:

$$\gamma(a) = - \frac{Z_1^v \varepsilon_1^{AA} + 2Z_2^v \varepsilon_2^{AA}}{2\sigma} \tag{3a}$$

$$\gamma(b) = - \frac{-Z_1^v \varepsilon_1^{AA} + 2Z_1^v \varepsilon_1^{AB} + 2Z_2^v \varepsilon_2^{AA}}{2\sigma} \tag{3b}$$

$$\gamma(c) = - \frac{Z_1^v \varepsilon_1^{AA} + Z_2^v \varepsilon_2^{AB}}{2\sigma} \tag{3c}$$

$$\Delta H_{sub}^{A} = \frac{1}{2}\left(Z_1 \, \varepsilon_1^{AA} + Z_2 \, \varepsilon_2^{AA}\right) \qquad (3d)$$

Here Z_1^{v} and Z_2^{v} are the numbers of vertical bonds (and Z_1 Z_2 are the total number of bonds) of first and second neighbors, respectively, ε_{12}^{AA} and ε_{12}^{AB} are the interaction energies for the first and second neighbors of pairs A-A and A-B. A corresponds to Fe while B represents Ni. Eq. (3d) expresses the heat of sublimation in terms of the interaction energies.

In a simplest estimate which neglects the second neighbor interactions, the interaction energies ε_1^{AA} and ε_1^{AB} can be easily found from the heats of sublimation and mixing [32], giving the values:

$$\varepsilon_1^{Fe\text{-}Fe} = -\ 103.48 \text{ kJ/mole}$$

$$\varepsilon_1^{Fe\text{-}Ni} = -\ 107.22 \text{ kJ/mole}$$

Estimates of the surfaces energies according to Eqs. (3a-c) are given in Table 1.

TABLE 1

	γ, mJ/m^2
(a) Free iron surface	γ_a = 4,139.0
(b) Ni on surface	γ_b = 4,439.4
(c) Ni below surface	γ_c = 4,139.0

The bond-breaking method is known [31] to overestimate the surface energies by a factor of 2; The experimental high temperature value of γ^{Fe} is 3,100 m J/m^2 [33]. The above simple estimate does predict that Ni atoms on the surface result in an increase of the surface energy. With only nearest neighbor interaction included, the Ni atoms below the surface, of course do not affect the surface energy (case (c) above).

LMTO-ASA Calculations

The scalar relativistic calculations were done on a uniform mesh of 50 points in the irreducible wedge of the tetragonal lattice for all supercells of Fig. 2.

As we mentioned earlier, LMTO-ASA-Stoner technique enabled us to calculate separately the nonmagnetic and magnetic contributions to the surface energies. The table below summarizes the corresponding results for supercells (a)-(c):

Table 2
SURFACE ENERGIES

	γ, m J/m^2	
	Total	Magnetic contribution
γ(a)	4,896	-666
γ(b)	5,298	-148
γ(c)	5,562	-678
γ(b)-γ(a)	402	518

As one can see, the ferromagnetic contributions to the surface energies are negative. Ni on the surface, case (b), makes the surface energy rise; this enhancement, is al entirely due to decrease in the magnetic contribution. The layer of Ni atoms below the surface, (c), results in even stronger effect, though the magnetic contribution in this case is virtually the same as in the pure iron surface (a).

The calculated magnetic moments of each atom presented in Table 3 provide further insight into the effect of Ni.

TABLE 3
MAGNETIC MOMENTS

Magnetic Moments μ_B/atom								
				Layers				
Supercell	C	S-4	S-3	S-2	S-1	S		
(a)	2.20	2.11	2.24	2.27	1.91	2.95		
						Ni ↓		
(b)	2.23	2.15	2.26	2.29	2.31	0.76		
					Ni ↓			
(c)	2.22	2.23	2.19	2.60	0.0	2.79		
		C			Ni ↓			C
(d)		2.26	2.08	2.52	0.0	2.52	2.08	2.26

First, in the pure iron surface, the magnetic moment of the surface atoms is almost 40% higher than that in the bulk. This effect was reported earlier [8,9] and is believed to be due to the emergence of a band of electronic surface states around the Fermi level. The oscillations of the magnetic moment we observe here had been also reported earlier [8,9], though very recent calculations by the FLAPW method do not confirm this result [35].

The drop in the magnetic contribution to the surface energy upon placing Ni on the surface results from the fact that the surface Ni atoms have a magnetic moment 4 times weaker than that of the Fe-atoms.

Ni in the bulk is only weakly ferromagnetic, as compared to Fe. In the stable FCC phase of Ni, m=0.56 μB/atom [36], while in the metastable BCC, m=0. 18 μB/atom [37]. The iron environment about the Ni-surface strongly enhances the magnetic moment. The obtained value of 0.76 μB/atom agrees very well with the recent result found from a spin-polarized calculation by FLAPW [38]. This enhancement however, should also be attributed to the electronic surface

states: unexpectedly, the iron environment in the bulk leaves Ni atoms nonmagnetic.

The two last lines of Table 3 show the distribution of magnetic moment in the layers for supercell (c) with Ni below the surface, and the reference supercell (d), where the layer of Ni-atoms is placed into the "bulk" environment of Fe. In both cases Ni is nonmagnetic ("C" in case (d) denotes the central Fe-layer - see Fig. 2).

From this table one can also see that substituting Fe for Ni on the surface strongly perturbs only the magnetic moment of the nearest Fe-layer, leaving those of the other layers virtually unchanged. The perturbation caused by the Ni layer below the surface is stronger. Note that the magnetic moments of the central layers ("C") of the four supercells: (a)-(d) are virtually equal to that of the Fe-atoms in the bulk BCC (2.2 μB/atom), which indicates that the dimensions of the supercells are adequate.

The obtained information on the surface energies can be used for estimating effective interatomic interaction energies. If only two shells of neighbors interact, then Eqs. (3a-d) are sufficient for calculating $\varepsilon_{1,2}$. (In Eq. (3d) $\Delta H_{sub}{}^{Fe}$=-413.798 KJ/mole [32]). Table 4 summarizes these results.

TABLE 4
INTERACTION ENERGIES FOR TWO SHELL NEIGHBOR MODEL

	Energy KJ/Mole	
	Fe-Fe ε	Fe-Ni ε
ε_1	-160.25	-164.02
ε_2	+75.7	+42.4

These results indicate that interatomic interaction potentials in Fe and Ni have oscillating character. The nearest neighbors attract each other, while the second neighbors undergo repulsive interaction. Interaction of the third neighbors is probably not negligible; however, the corresponding potentials cannot be calculated from the data

available, unless a hypothesis is adopted regarding the ratio $\varepsilon_3/\varepsilon_2$.

The surface energies we calculated from the LMTO-ASA method agree in general with those found from the simple near neighbor bond-breaking arguments. Like the latter, they are some factor of 1.5 greater than the experimental values. The discrepancy of the bond breaking values is most probably due to the fact that the total energy (or the heat of sublimation) is not, in fact, just the sum of interaction energies. A constant, volume-dependent term should be added. On the other hand, the main source of overestimate of the LMTO-ASA surface energies is probably in poor approximation of vacuum by empty spheres and neglecting lattice relaxation effects. The degree of overestimation is not certain, however, as the actual low temperature surface energy (and Griffith fracture work) may be much higher than indicated by high energy experiments due to the absence of the entropy contributions important at elevated temeperatures.

CONCLUSIONS

In applying our results to the problem of cleavage on the (100) plane in BCC iron, one may conclude that ferromagnetism is a major factor in resistance to decohesion on this plane. The surface energy has a strong negative magnetic component. Atoms of Ni on the iron surface are much less ferromagnetic, and thus appreciably increase the surface energy and (Griffith fracture work) due to lowering the magnetic contribution. The surface energy increases even more strongly if Ni is present below the surface. This effect, however, is purely chemical: the overall magnetic contribution to the surface energy is virtually the same as in the case of the pure iron surface. The Ni-atoms below the surface are nonmagnetic. Although actual surface energy predictions are not yet in good agreement with experiment the predicted trends with Ni atom positions offer valuable insight into the electronic basis of a technologically important alloying effect on fracture toughess.

Further calculations using these methods are now being directed at the mechanism of phosphorus embrittlement of Fe grain boundaries. Supercells have now been constructed for this problem (39) and initial calculations indicate large magnetic contributions to the grain boundary energy in Fe. From an understanding of the electronic basis of P embrittlement, further calculations could guide the design of multicomponent

grain boundary compositions to exploit ternary electronic interactions enhancing boundary resistance to embrittlement by impurities including hydrogen. Design at this level offers the greatest potential for major property advances.

ACKNOWLEDGMENTS

This work has been performed as a part of the Steel Research project sponsored by National Science Foundation Grant No. 8418718DMR. The collaboration with the Center for Materials Research of Los Alamos National Laboratory is gratefully acknowledged. The LANL CRAY supercomputers have been used; we greatly appreciate the valuable assistance of the consultants office of the LANL computer center, especially that of Mr. Robert Frank. It is also a pleasure to acknowledge the fruitful discussion with Prof. A. Freemen of Northwestern University. The LMTO-ASA computer code developed by N. Christensen has been used in all calculations.

References

1. O.K. Andersen, Phys. Rev. B12, 3060 (1975).

2. O.K. Andersen in "Electronic Structure of Complex Systems"(ed. P. Phariseau and W.M. Timmerman), Plenum 1984.

3. O.K. Andersen, O. Jepsen, D. Gloetzel in "Highlights of Condensed Matter Theory" (Ed. F. Bassani, F. Fumi, P.M. Tosi). North Holland, 1985.

4. H.L. Skriver, The LMTO Method. Springer, 1984

5. K.B. Hathaway, H.F. Jansen, A.F. Freeman, Phys. Rev. B31, 7603 (1985).

6. V.L. Moruzzi, P.M. Markus, K. Schwarz, P. Mohn, Phys. Rev. B34, 1784 (1986).

7. D.G. Dempsey, L. Kleinman, Ed. Caruthers, Phys. Rev. B12 2932 (1975).

8. G.S. Wang, A.F. Freeman, Phys. Rev. B24, 4364 (1981).

9. S. Ohnishi, A.F. Freeman, Phys. Rev. B28, 671 (1983).

10. T. Oguchi, A.F. Freeman, J. Mag. Magn. Matls. 54-57, 797 (1986).

11. C.L. Fu, A.F. Freeman, Phys. Rev. B33, 7322 (1986).

12. C.L. Fu, A.F. Freeman, Phys. Rev. B33, 925 (1987).

13. R.P. Messmer, C.C. Briant, Acta Metall. 30, 457 (1982).

14. C.L. Briant, R.P. Messmer, Acta Metall. 30, 1811 (1982).

15. C.L. Briant, R.P. Messmer, Acta Metall. 32, 2043 (1984).

16. M. Hashimoto, Y. Ishida, R. Yamamoto, M. Doyama, T. Fujiwara, Surface Sci. 144, 182 (1984).

17. M. Hashimoto, Y. Ishida, R. Yamamoto, M. Doyama, Acta Metall. 32, (1984).

18. M. Mori, Y. Ishida, in Proceedings of JIMIS-4 (1986), p361.

19. M. Eberhart - This Proceedings.

20. M. Eberhart, D.D. Vvedensky, in "Chemistry and Physics of Fracture" (ed. by R. H. Jones and R.M. Latanision) M. Nijhoff, Hingham, MA 1987.

21. P. Hohenberg, W. Kohn, Phys. Rev. 136, B864 (1964).

22. W. Kohn, L.R. Sham, Phys. Rev. 140, A113 (1965).

23. E.C. Stoner, Proc. R. Soc. London, Ser. A 169, 339 (1939).

24. F. Madsen, O.K. Andersen, U.K. Poulsen, O. Jepsen, in "Magnetism and Magnetic Materials" (Ed. H.C. Wolfe), Philadelphia, 1975

25. U.K. Poulsen, J. Kollar, O.K. Andersen, J. Phys. F6, L241 (1976).

26. O.K. Andersen, J. Madsen, U.K. Poulsen, O. Jepsen, J. Kollar, Physica, 86-88B, 249 (1977).

27. G.L. Krasko. Phys. Rev. B36, 8565 (1987).

28. G.L. Krasko, G.B. Olson, Phys. Rev. B40, 11536 (1989).

29. O. Gunnarsson, J. Phys. F6, 587, (1976).

30. J.J. Janak, Phys. Rev. B16, 255 (1977).

31. P. Wynblatt, R.C. Ku, in "Interfacial Segregations" (ed. W.C. Johnson, J.M. Blakely), ACM, 1977.

32. R. Hultgren, P.A. Desai, D.T. Tawkins, M. Gleiser, K.K. Kelly, "Selected Values of the Thermodynamic Properties of Binary Alloys. AMS, 1973.

33. As quoted in J.R. Smith, A. Banerjea, Phys. Rev. Lett. 59, 2451 (1987).

34. C.L. Fu, A.J. Freeman, T. Oguchi, Phys. Rev. Letters 54, 2700 (1985).

35. A.J. Freeman, Private Communication.

36. H. Dannan, R. Kerr, A.J.P. Meyer, J. Appl. Phys. 39, 669 (1968).

37. G.L. Krasko, unpublished.

38. J.I. Lee, C.L. Fu, A.J. Freeman, to be published.

39. R.J. Harrison and F. Spaepen, This conference.

MECHANISMS FOR CLEAVAGE AND INTERGRANULAR EMBRITTLEMENT IN FE

M.E. Eberhart*[1,2] and J.M. MacLaren[3]

(1) *Materials Science and Technology Division, Los Alamos National Laboratory, Los Alamos, NM 87545, USA.*

(2) *Department of Materials Science, Massachusetts Institute of Technology, Cambridge, MA 02139*

(3) *Theoretical Division, Los Alamos National Laboratory, Los Alamos, NM 87545, USA.*

ABSTRACT

The mechanism of cleavage in bcc Fe has been investigated with electronic structure calculations and compared to similar calculations modeling cleavage in other bcc materials (Li, Nb, Mo). It has been found in the bcc materials we have studied that those known to undergo (100) cleavage show enhancement of the density of states (DOS) on the virtual surface layer as the material is strained to failure. Using total energy calculations it is shown that there is a point of inflection (corresponding to the point of maximum force versus displacement) in the total energy at nearly the same point as the maximum enhancement in the DOS. We conjecture that this point represents the transition state for the fracture process. Extending these ideas, the electronic structure near a Fe(111) grain boundary has been calculated both with and without segregated P. We find clear evidence for the formation of a P band of states, suggesting the existence of P-P interactions within the segregated layer. A chemical model of strain-induced bond failure is suggested in which bonds parallel to the fracture surface compete with the cohesive Fe-Fe bonds normal to the surface.

INTRODUCTION

Our approach to the study of mechanical behavior of metallic materials, and to the study of fracture in particular, has been to use first principles quantum mechanical calculations to study the electronic structure of a host of materials which exhibit a variety of mechanical responses. Then correlations between the known mechanical properties and features observed in the calculated electronic properties are used to provide a microscopic understanding. This is an extension of the method by which the structure property relationships of metallurgy were established and represents an extension from the recovery of relationships between crystal structure and properties.

Until recently, a first principles study of fracture has been complicated by an inability to model the fracture process. Therefore, the correlations which have been established are between features of the intrinsic mechanical behavior and the electronic structure of the starting (unfractured) material (1). By far the more interesting and technologically rewarding area of investigation is the electronic evolution

associated with the fracture process. It is, after all, the competition between the evolution of a crack and the emission of a dislocation which represents the deformation process. Therefore an initial understanding of the changes in the electronic structure accompanying cracking is an area which must be studied before a complete electronic understanding of deformation can be obtained.

In this paper we use the layer Korringa-Kohn-Rostoker (LKKR) electronic structure technique (2,3,4) to study the evolution of the (100) cleavage process in bcc Fe and the properties of an ideal Fe(111) grain boundary and the electronic influence of segregated P impurities at this boundary. The LKKR approach provides an accurate and elegant solution to the Schrödinger equation, within the self-consistent field and local spin density approximations, for an infinite solid and only assumes translational symmetry in two directions. The method models an isolated defect by embedding a slab containing the defect in two semi-inifinite bulk regions and since Fe is magnetic, allows spin-polarization of both bulk and interface regions. The mathematical details and physical approximations involved in LKKR interface calculations are discussed in detail inRefs. (2,3,4), and rather than reproduce the details here, we refer the reader to these papers. The technique is thus ideally suited for studying interfaces in bulk materials such as the (111) grain boundary as well as the cleavage process.

RESULTS

- *(100) cleavage of Fe*

The initial studies of cleavage on the (100) planes of Fe were undertaken by modelling a simple interface in which only two interplanar spacings were expanded from the bulk. This geometry is shown schematically in Fig. 1.

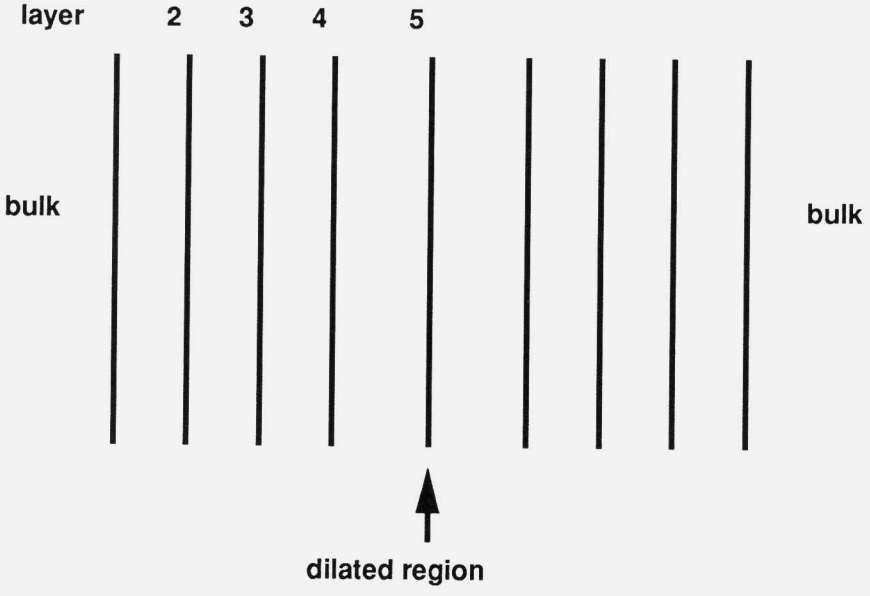

Figure 1: Interface chosen to model (100) cleavage

Fig. 2a: Fe cleavage 10% expansion

spin up

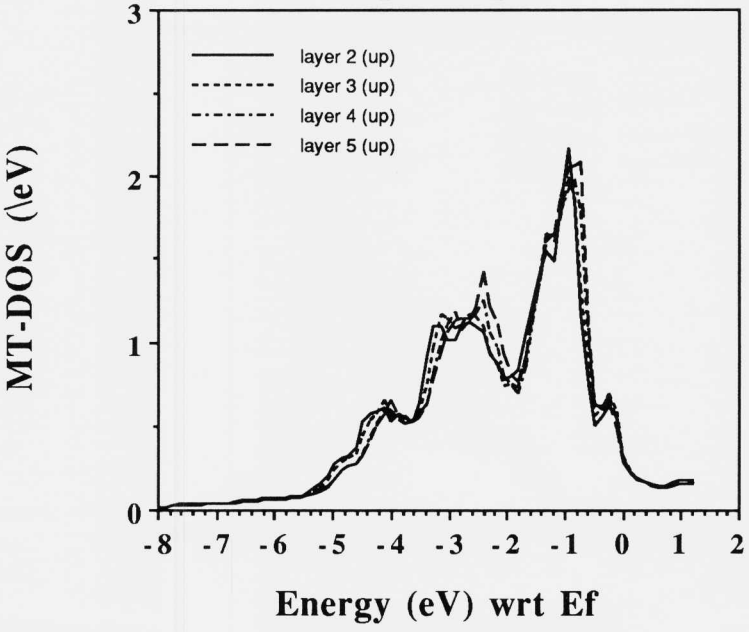

spin down

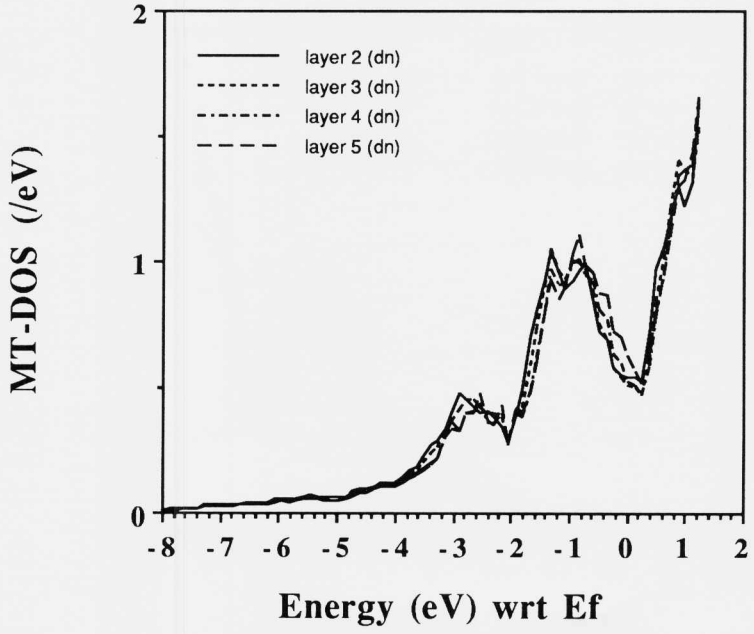

Fig. 2b: Fe cleavage 30% expansion

spin up

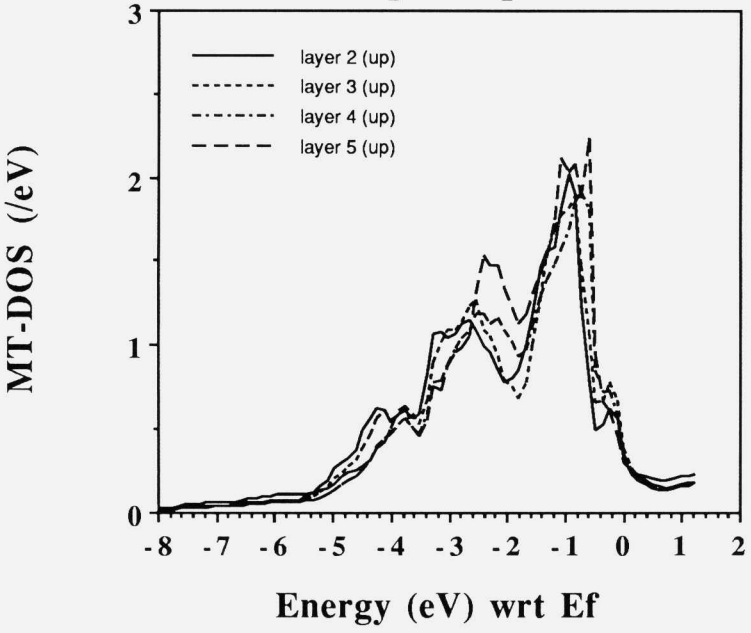

spin down

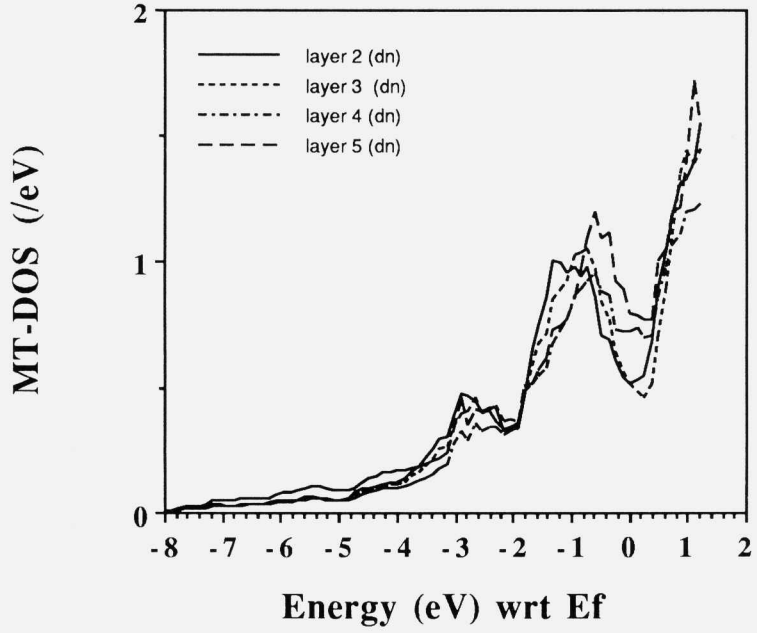

Fig. 2c: Fe cleavage 42% expansion

spin up

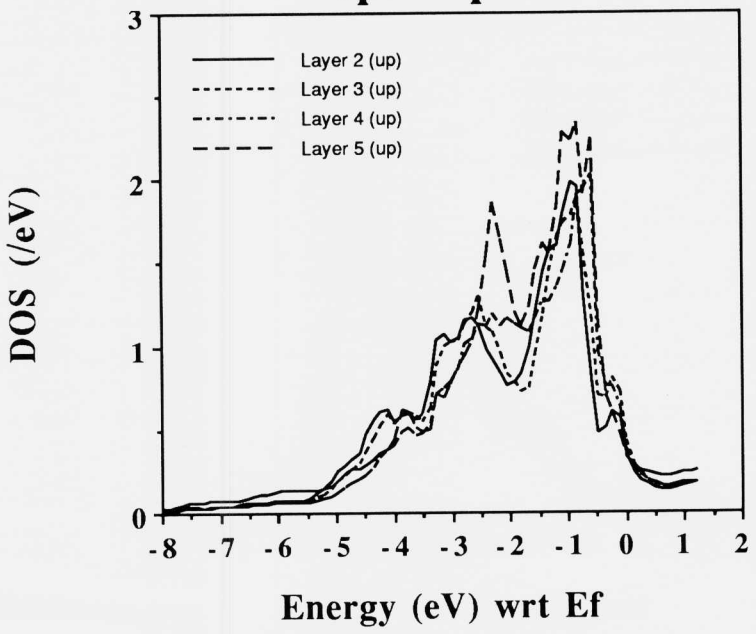

spin down

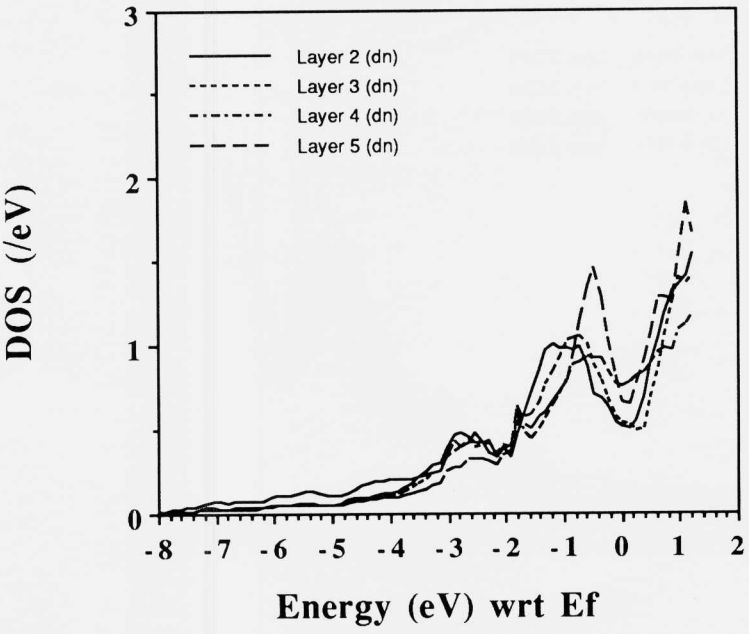

Fig. 2d: Fe cleavage 50% expansion

spin up

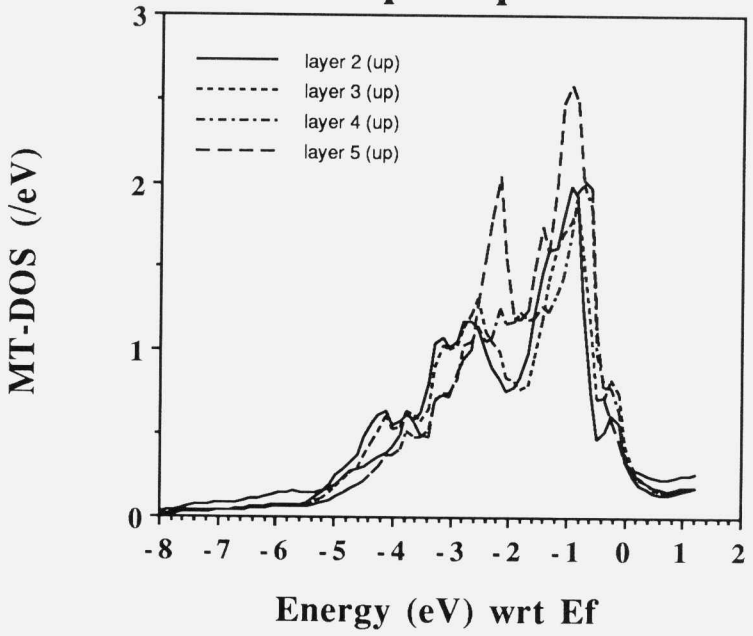

spin down

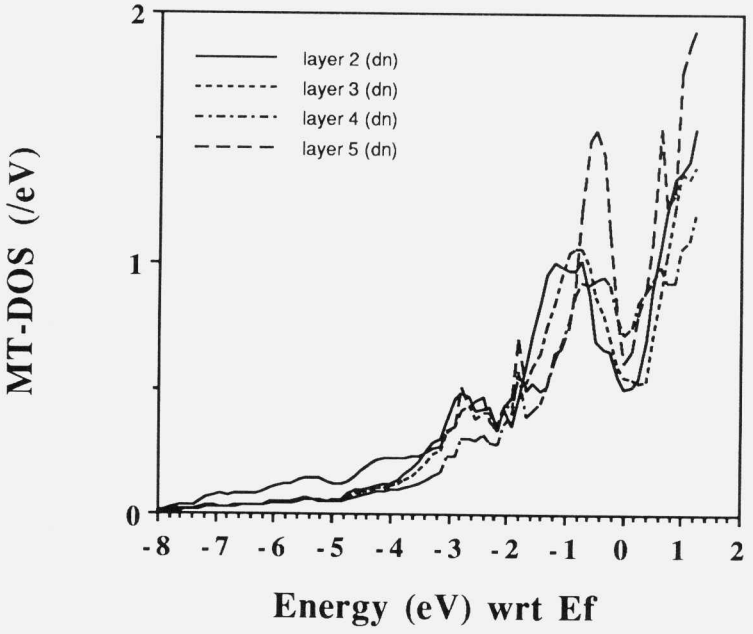

Four calculations have been performed corresponding to expansions between layers 4 and 5 of 10%, 30%, 42% and 50% over the bulk interplanar spacing. The DOS for each of the layers as a function of separation for both majority and minority spins is shown in Fig. 2. Beginning with the initial dilation of 10% (Fig 2a) the DOS near the Fermi energy on the center layer (layer 5) is enhanced relative to the bulk, this is particularly apparent on the spin down band. This enhancement is maximum somewhere between 30% and 42%. (Figs. 2b and 2c) The 42% expanded layer spacing (Fig. 2d) produces a central three layer region where the structure is rigorously fcc. We have postulated in a previous work (5), using ideas suggested by Bader *et al.* (6) for identifying bonds from structures in the total charge density, that by symmetry fcc crystals only have first neighbor bonds though bcc crystal have both first and second neighbor bonds. Thus the 42% expansion corresponds to the breaking of the second neighbor (100) bonds, present in all bcc materials, at the interfacial layer and should correspond to the maximum in the force versus displacement curve. To confirm this, the total energy for the four layer separations has been computed and is shown graphically in Fig. 3. We expect the maximum in the force versus displacement curve to correspond to a point of inflection in the total energy versus separation curve of Fig. 3. As is clearly seen such an inflection point exists between the 30% and 42% dilations. Further confirmations is provided in Fig. 4, where the electronic pressure, which corresponds to an average pressure, is plotted. A maximum in the electronic pressure is seen at approximately the same expansion as the inflection point in the total energy.

We take all of this information as a strong indication that the maximum in the force versus displacement curve occurs near an interlayer spacing where the coordination is locally fcc and thus the second neighbor bonds that exist, by symmetry within the bcc structure are being broken. At this interlayer spacing, we postulate, that the second neighbor bonds parallel to the virtual fracture surface are competing with the second neighbor bonds across the fracture surface. At greater interlayer spacing the formation of bounds parallel to the surface are energetically more favorable than those across the interface and serve to lower surface energy. Hence the point of maximum strain during (100) cleavage is the point where bonds normal to the fracture surface are exactly compensated by bonds parallel to the fracture surface. This conjecture is consistent with the enhancement of the DOS near the Fermi energy (E_F) on the forming surface layer. An enhancement of the DOS near E_F is a feature we associate with the changes in bonding from perpendicular to parallel to the interface resulting from the lifting of degeneracy along (100) directions by the strain. In an alternative picture, the DOS near E_F is a measure of the susceptibility of a system to respond to some external perturbation. In our case the external perturbation is a stress and the response is a strain. The enhancement of the DOS near E_F on the central layer suggests that the atomistic mechanism for cleavage is strain localization to the atomic bonds across cleavage plain. In the limit of infinite separation, two free surfaces are formed in which atomic relaxations at these surfaces will be small compared to that between the surfaces. Thus the strain can be thought of as fully localized between these two surfaces.

Fig 3: Total Energy vs Separation

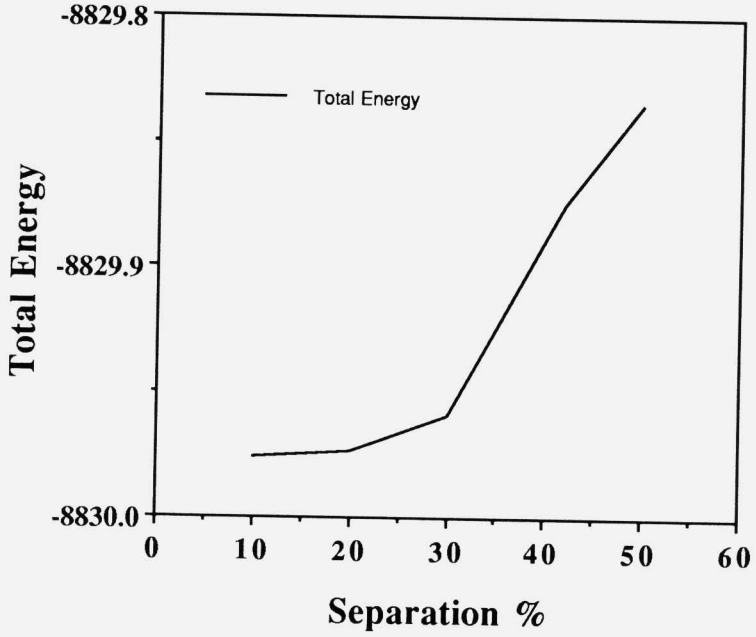

Fig 4: Pressure vs separation

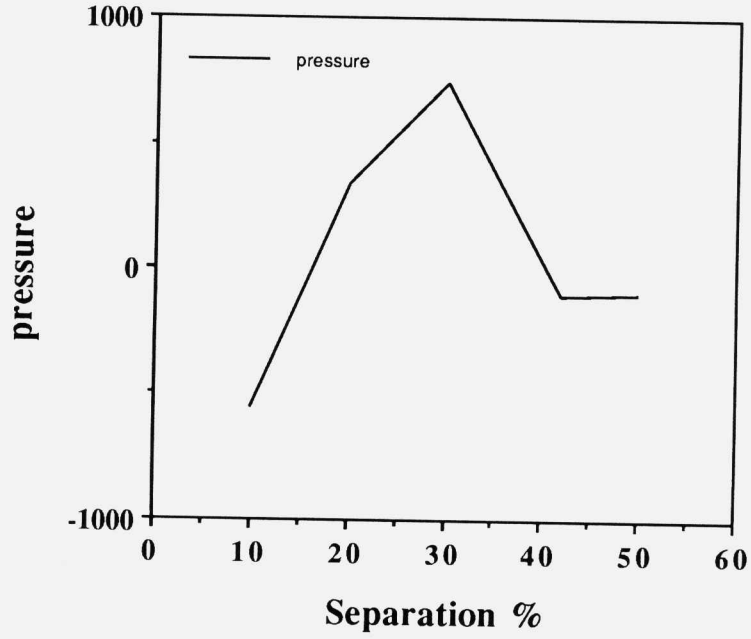

• *Electronic Structure near a (111) grain boundary in Fe*

If all fracture, including environmentally induced embrittlement, is to occur by similar atomistic mechanisms then we may expect that fracture in general is the result of a competition between bonds normal and parallel to a virtual fracture surface. Further, the point of maximum bond strain should be characterized by states crossing E_F, signified by some enhancement in the DOS near E_F, as in the cleavage example discussed above. Extending these ideas, a Fe (111) grain boundary with and without segregated P has been investigated with the LKKR approach. The unrelaxed Σ 3 grain boundary structure which we have examined is formed by joining a stack of (111) planes with its mirror image. The P atoms are placed in the centre of the trigonal capped prisms formed at the grain boundary. This site gives a hard sphere radius to be almost identical to that of the P covalent radius, thus we expect this to be the likely segregation site at this boundary.

In accordance with our conjecture we expect that if P embrittles this (111) boundary then we would find some enhancement of the DOS near E_F on the boundary layer. Accordingly, Fig. 5 shows the DOS for this grain boundary with (Fig. 5b) and without (Fig. 5a) segregated P. There is significant contraction of the d-bands at the boundary which is a direct result of the reduced coordination at the boundary. As a consequence, the magnetic moment is enhanced from the bulk value of 2.2μB to 3.6μB at the boundary layer. Fig. 5a shows a small enhancement of the DOS near E_F on the boundary layer in the minority band only. The influence of P on the Fe(111) boundary is shown in (Fig. 5b). The DOS for the interface layer is broken down into P and Fe contributions. On summing these two contributions we find an enhancement in the minority DOS near E_F on the boundary layer (layer 4). There is also significant P-P and Fe-P interactions as evidenced by both the peak at -10eV in the P DOS and the broad band features between 0 and -6eV of E_F. As expected, the influence of the P atoms on the magnetic properties of this boundary is to dramatically reduce the moment to 2.6μB by forming Fe-P bonds. The effect of the P impurities is to form P-P and Fe-P bonds which will be predominantly parallel to the interface, suggesting a weakening of the interface. The overall features of this boundary are similar to those seen in both LKKR and cluster calculations on Ni(210) boundaries both with and without segregated S (7). The analogy with the (100) cleavage of Fe would be the formation of P-P and P-Fe bonds parallel to the boundary that compete with Fe-Fe bonds normal to the boundary. This places a strong constraint on the geometry at a brittle boundary. If we assume that P will occupy the interstices of trigonal capped prisms then a condition for a brittle boundary would be that these trigonal prisms shared edges within the boundary. Thus strain normal to the boundary will create a condition in which the formation of P-P bonds parallel to the boundary complete with the strained Fe-Fe bonds normal to the boundary. Note the formation of the P-P bonds parallel to the boundary will also act to lower the surface energy, thus promoting the tendency for P to embrittle Fe.

Fig 5a: Fe (111) 7 layer grain boundary

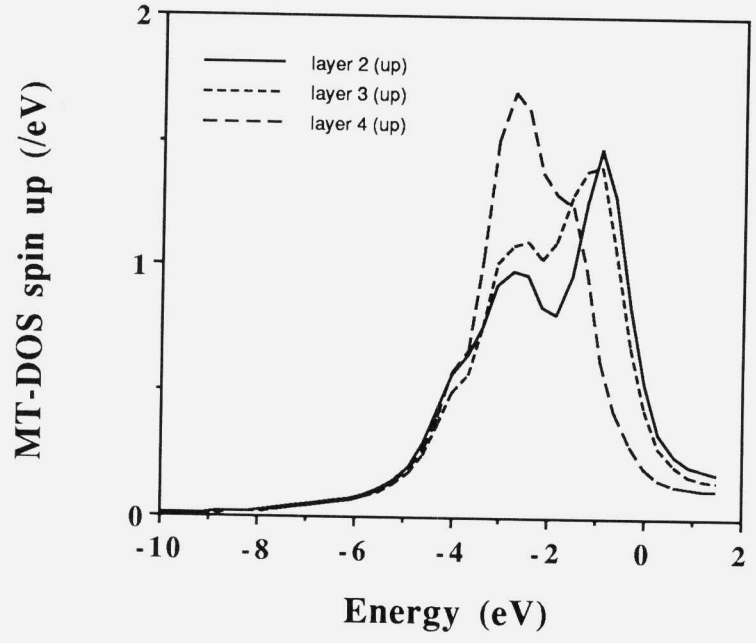

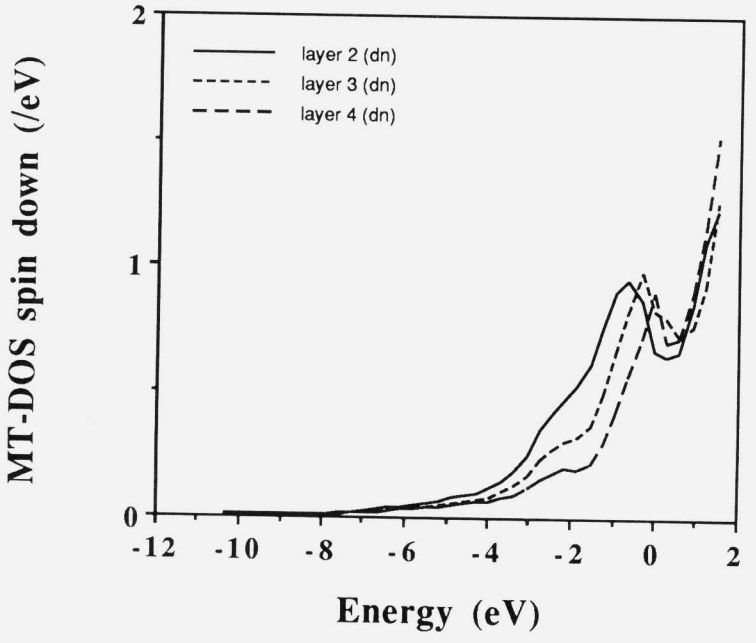

Fig 5b: Fe (111) + P 6 layer grain boundary

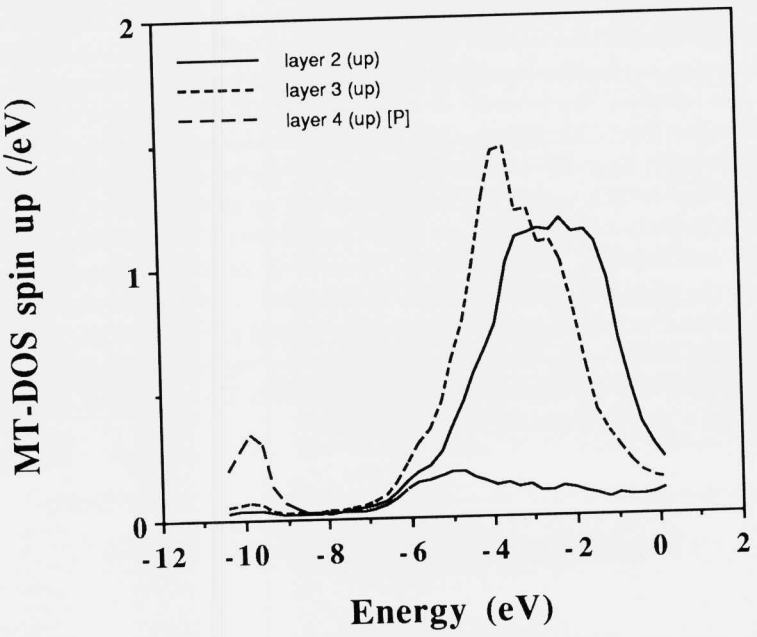

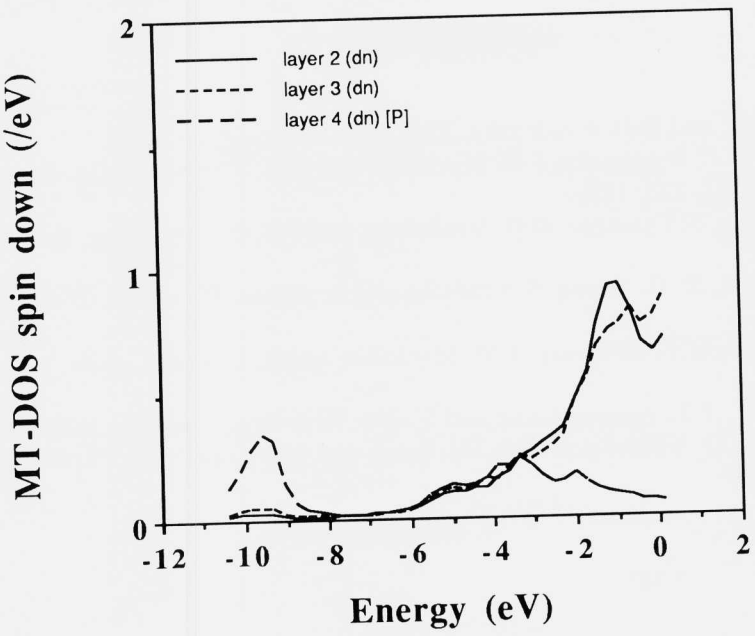

CONCLUSIONS

The electronic structure of simple geometries representing an Fe(111) grain boundary and Fe(100) cleavage has been calculated with the spin polarized LKKR technique. In the cleavage calculations we find that the point of inflection in the energy as a function of separartion is close to the point where, by symmetry, the second neighbor bcc bonds at the interface are broken. A signature for this is an enhancement of the electronic DOS near E_F. Calculations are currently under way to test whether a significantly different DOS near E_F can be generated by packing polyhedra containing segregated impurities which either are noninteracting or share corners, edges, or faces. In the grain boundary calculations, we find clear evidence for the formation of both P-P and P-Fe interactions, suggesting the weakening of the interface by preferential bonding in the plane of the interface. A chemical model of strain-induced bond failure is suggested in which impurity-impurity bonds parallel to the fracture surface compete for the cohesive Fe-Fe bonds normal to the surface. Such a situation is conjectured to produce the enhancement of the DOS near E_F consistent with the changes thought to be a prerequisite for brittle failure.

ACKNOWLEDGEMENTS

This work was supported by the Office of Naval Research, the Department of Energy and the National Science Foundation.

REFERENCES

1. M.E. Eberhart and D.D. Vvedensky, *Phys. Rev. Lett.*, 58, 61, 1987.
2. S. Crampin, D.D. Vvedensky, J.M. MacLaren and M.E. Eberhart, *Mat. Res. Soc. Symp. Proc.* 141, 373, 1989.
3. J.M. MacLaren, S. Crampin, D.D. Vvedensky and J.B. Pendry, *Phys. Rev. B*, in press, 1989.
4. J.M. MacLaren, X.-G. Zhang, S. Crampin and A. Gonis, *Phys. Rev. B*, in press, 1989.
5. M.E. Eberhart, M.E. McHenry, J.M. MacLaren and S. Crampin, *Acta. Met.*, in press, 1989.
6. R.F.W. Bader, T.T. Nguyen-Dang and Y. Tal, *Rep. Prog. Phys.* 44, 893, 1981.
7. S. Crampin, D.D. Vvedensky, J.M. MacLaren and M.E. Eberhart, *Phys. Rev. B* 40, 3413, 1989.

A NOVEL HYDROGEN-RESISTANT UHS STEEL

JOHN F. WATTON, GREGORY B. OLSON, MORRIS COHEN
Department of Materials Science and Engineering,
Massachusetts Institute of Technology, Cambridge, MA
02139.

INTRODUCTION

Ultrahigh-strength martensitic steels tempered to a high hardness (stage one) are extremely sensitive to environmental effects. Catastrophic failures of structural components by intergranular stress-corrosion cracking have resulted in loss of life and extensive property damage. The mechanism of failure is believed to be hydrogen embrittlement from cathodic charging of the crack tip (1), and grain-boundary segregation of certain tramp elements and alloying elements are known to promote this condition. The solution to this problem is a new class of high-strength steels relatively insensitive to environmental effects.

Bandyopadhyay et al.(2) have shown the effect of reducing concentrations of certain elements on the threshold stress intensity for hydrogen stress-corrosion. Below a total of about 0.2 wt.% of Mn, Si, and P, a significant improvement in the threshold is achieved in a 4340-type steel with a yield strength of 1450 MPa. Banerji et al. (3) further showed that a small improvement is realized in high-purity 4340 (low P and S), and a very impressive fivefold improvement by eliminating Mn and Si. The effect of chromium on intergranular stress-corrosion cracking has not been clearly established, but there is evidence through thermodynamic calculations by Lee et al.(4) and Seah (5) that the presence of chromium will increase grain-boundary embrittlement.

Rare earth additions have been successful in improving the resistance of many steels to temper embrittlement by effectively gettering tramp elements (6,7,8,9). Other research (4,10,11,12) demonstrates that reducing chromium, manganese, and silicon which are believed to interact with tramp elements, phosphorus in particular, also improves

resistance to temper embrittlement. The resistance to intergranular stress-corrosion is likewise improved by a reduction of these elements (2,3,13,14,15), but the gettering of phosphorus is more difficult because the concentration of P which promotes stress-corrosion cracking in stage-one tempered martensitic steels is 1 to 2 orders of magnitude lower than the level causing temper embrittlement. It is therefore necessary to produce a phosphorus compound with the lowest solubility product (highest thermodynamic stability) to effectively getter low concentrations. Highly reactive gettering agents are necessary to form these compounds, but during conventional solidification the principal products tend to be relatively coarse oxide and oxysulfide particles; however, via rapid solidification processing (RSP) the gettering agent reacts to form a fine dispersion of oxysulfide and metastable phosphorus compounds.

Recent research (16) on RSP of certain steels reported a remarkable resistance to high-temperature grain growth compared with the same alloy processed conventionally. This stability was attributed to grain-boundary pinning by a fine dispersion of sulfide particles refined by RSP. It was then proposed (16) to take advantage of this phenomenon to improve sharp-crack fracture toughness of ultrahigh-strength steels by high-temperature austenitizing (900°C-1200°C). The result would be the dissolution of void-initiating carbides without the loss of blunt-notch toughness and tensile ductility normally associated with grain coarsening. Furthermore, in line with the fine grain size a reduction of the ductile-brittle transition temperature was observed in RSP steels (17). A subsequent study (18) suggested that optimum grain-coarsening resistance is afforded when the second-phase dispersion has the lowest solubility in the matrix. A thorough study of dispersed phases in conventional and RSP matrix steels by Hsu (19) emphasized the potential of RSP to produce fine dispersions of classical phases as well as creating new metastable compounds resistant to dissolution at high processing temperatures.

The present research (20) is a synthesis of previous and on-going work in processing/structure/property relationships to improve the resistance to

intergranular stress-corrosion cracking in stage-one tempered martensitic steel. Combining the benefits of RSP, late additions of highly reactive gettering elements, and careful alloy selection, a novel ultrahigh-strength RSP Ni-Mo-La steel has been designed, processed, and evaluated. An extensive review of available thermochemical data has been conducted and simple thermodynamic and kinetic models were used to select a gettering element and to predict the likely products of sulfur and phosphorus. These fine dispersions of highly stable compounds then provide grain-coarsening resistance during high consolidation and austenitizing temperatures to maximize both mechanical properties and stress-corrosion cracking resistance. The results of this work are capable of providing a new class of high-strength martensitic RSP steels.

Ni-Mo-La STEEL ALLOY DESIGN

Choice of Gettering Agent

A detailed review of the thermochemical literature (21-27) was carried out and changes in standard state were made to the 1 wt.% reference infinitely dilute solution in liquid iron at 1600°C. Table 1 lists selected compounds of phosphorus and sulfur which are considered promising candidates.

TABLE 1

Selected Phosphorus and Sulfur Compounds

Phosphide	Phosphate	Sulfide	Oxysulfide
LaP	$LaPO_4$	LaS	La_2O_2S
CeP	$CePO_4$	CeS	Ce_2O_2S
ThP	$ThPO_4$	ThS	ThOS
YP	YPO_4	YS	Y_2O_2S
		US	UOS
			ZrOS

From this group La and Ce were chosen as the best gettering elements based on available data. The free energy of formation for the phosphates is approximated by comparison of the relationship

between AlP, Al_2O_3, and $AlPO_4$ which have known free energies of formation in liquid iron. LaP, CeP, La_2O_3, and Ce_2O_3 free energies are also known, and the phosphate is estimated by assuming $LaPO_4$ and $CePO_4$ have a relative stability between the phosphide and oxide as in the Al-P system. A secon method of approximation described in reference (22) gave good agreement. These data are summarized in Figure 1 where the rare earth phosphates are given as dashed lines to indicate their uncertainty.

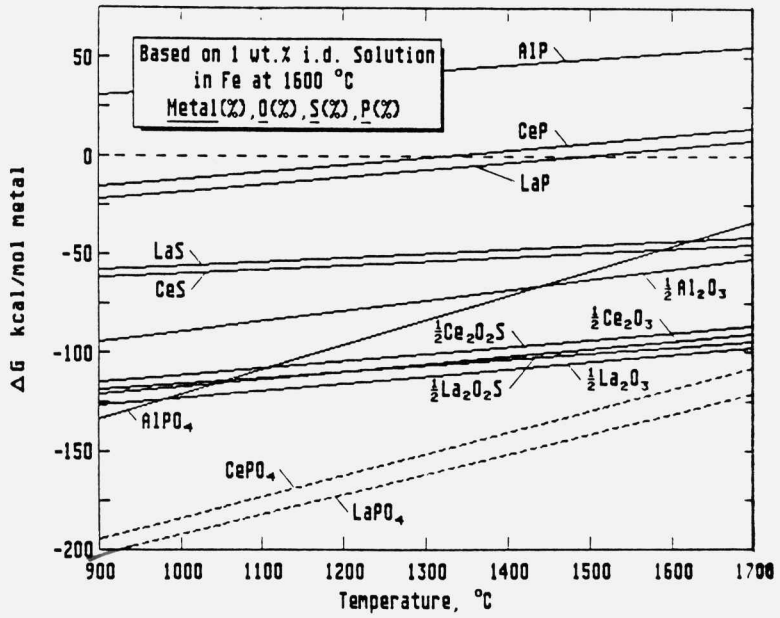

Figure 1. Free energy of formation vs. temperature on a mole metal basis for the metal, O, S, and P in solution at 1600°C.

It is important to emphasize that the free energy i extrapolated from the liquid iron (1500°C-1700°C) t the austenitizing temperature range (900°C-1200°C) for relative comparison of compounds where large differences in free energy exist. It is expected that there may be significant differences in the solid-state solution thermodynamics which would mak comparison at small differences in free energy erroneous. The primary concern in this analysis is

to assess the likely compounds that may form in liquid iron from a superheat of 1650°C to a supercooled liquid, and at low concentrations of phosphorus and sulfur.

The relative stability of each compound is dependent upon the Henrian activity of the species present. Only certain compounds were chosen which reflect the likely conditions in the melt at low concentrations of phosphorus and sulfur. For example, there are three known compounds of sulfur in the binary cerium system, CeS, Ce_3S_4, and Ce_2S_3. It is not expected that Ce_3S_4 and Ce_2S_3 will precipitate under experimental conditions at low concentrations of sulfur. A further analysis also suggests that except at very high sulfur concentrations and very low oxygen concentrations, Ce_2O_2S is more stable than CeS. Therefore, two rare earth (RE) systems have been chosen, Fe-RE-O-S and Fe-RE-O-P, with the appropriate phases of RES, RE_2O_2S, RE_2O_3, REP, and $REPO_4$. The RE element La was selected based on results presented in Figure 1 which indicates its greater gettering strength over Ce. It is not possible to predict phase precipitation from thermodynamics alone. In the discussion section, nucleation kinetics will also be considered.

Alloy Composition

The composition specifications are intended to produce a novel ultrahigh-strength martensitic structural steel with high hardenability and resistance to stress-corrosion cracking. Table 2 compares the new alloy composition and 4340 steel; the latter represents the strength and hardenability desired, but lacks resistance to stress-corrosion at high hardness. The carbon concentration was held constant at 0.40% to provide the strength and hardness in the stage-one tempered condition. Nickel was increased to 2.00%, representing the high side of the 4340 range, for cleavage resistance. The grain-boundary Ni-P interaction is believed to be weak and of little consequence when compared with the benefit of Ni to fracture toughness. Molybdenum was increased to 1.5% to offset the loss in hardenability by the reduction of Mn, Si, and Cr which are believed to promote segregation or co-segregation with P and S. Based on simple

thermodynamic models (4,5), molybdenum is expected to enhance intergranular cohesion. The high

TABLE 2

Ni-Mo-La Steel Alloy Composition

Element, wt%	Ni-Mo-La Steel	4340 Steel
C	0.40	0.38-0.43
Ni	2.00	1.65-2.00
Mo	1.50	0.20-0.30
Mn	<0.01	0.60-0.80
Si	<0.01	0.15-0.30
Cr	<0.01	0.70-0.90
P	0.005	0.035 max
S	0.005	0.040 max

molybdenum concentration is not expected to result in a segregation problem because, through rapid solidification, the fine micro-segregation that does occur will be readily homogenized during hot consolidation due to the short diffusion distances. The grain-coarsening resistance of RSP steels should allow use of the higher solution treatment temperatures required to dissolve molybdenum carbides in this composition.

Phosphorus and sulfur were kept low deliberately in the steelmaking and their concentrations in solution were then further reduced by the gettering effect of lanthanum. The lanthanum additions were based on the concentrations of phosphorus and sulfur together with the anticipated loss due to melt crucible and atmosphere interaction. The following mass balance modified to account for processing losses represents the total lanthanum addition:

$$\%La_{ADD}=[8.7(\%S)+4.5(\%P)][1+\%Loss/100] \qquad (1)$$

where 8.7 is the stoichiometric factor for La_2O_2S and 4.5 corresponds to LaP or $LaPO_4$. The %Loss in the processing factor is assumed to be 50% and will be discussed further in the next section. The lanthanum addition was made as $LaNi_5$. This compound

has a low melting temperature and excellent solution characteristics in liquid iron.

Process Design

The highly reactive nature of lanthanum as a gettering agent requires careful attention during the process to prevent excessive melt/crucible and melt/atmosphere interactions. The %Loss for lanthanum additions represented in equation 1 is reported to range between 20% and 80%, depending upon processing. The atmosphere, crucible material, holding time after the late addition, and surface area to volume ratio of the melt are major considerations. In this work, the %Loss, based on an alumina crucible under the processing described was expected to be about 50% and the reaction products should include Al_2O_3, $LaAlO_3$ and La_2O_3.

EXPERIMENTAL PROCEDURE

Processing

The Ni-Mo-La steel alloy was processed at Pratt and Whitney's centrifugal atomization facility in West Palm Beach, Florida. Two ingots, produced by Republic/LTV Steel, were remelted and centrifugally atomized in the 15 kg (33 lb.) capacity unit. The processing procedure included remelting of the ingots, superheating to 1650°C, making the $LaNi_5$ addition, holding for 2 minutes, then atomizing in helium. Powder consolidation was accomplished by hot extrusion at 1100°C with a 20:1 reduction in area. A small quantity of powder was HIP'ed at 1100°C for 2 hours at 30 000 psi for preliminary study of hardness response to heat treatment, grain-coarsening resistance, and STEM analysis of second-phase particles.

The HIP'ed bar was austenitized at 900°C, 1100°C, and 1300°C for 1 hour, oil quenched, and tempered 1 hour at 200°C. Extruded samples for hardness evaluation were austenitized at 900°C, 1000°C, 1100°C, and 1200°C for 1 hour, oil quenched, and tempered 1 hour at 125°C, 150°C, 175°C, and 200°C. Tensile specimens were austenitized at 1100°C for 1 hour, oil quenched, and tempered 1 hour at 150°C, 175°C, and 200°C. K_{IC} and K_{ISCC} test

specimens were austenitized at 1100°C for 1 hour, oil quenched, and tempered 1 hour at 200°C.

Mechanical Testing

Hardness measurements were made on the HIP'ed samples using a Vickers micro-hardness machine (diamond pyramid hardness) where multiple readings were taken across the diameter. Rockwell C hardness was taken on all extruded test samples and mechanical test specimens. The tensile bars were first machined into blanks, heat treated, then final ground to ASTM specifications. The K_{Ic} and K_{Iscc} specimens were of the half-size Charpy design. Blanks were machined, heat treated, then finish ground and V-notched. Fatigue pre-cracking was performed on an Instron Hydraulic Servo Fatigue machine according to the ASTM standard E399. Tensile tests were conducted using an Instron testing machine with a crosshead speed of 0.02"/min. and a 20 000 lb. load cell. Yield strengths were measured at 0.2% offset according to ASTM standards. K_{Ic} specimens were tested on the same machine in a 3-point bend configuration at a crosshead speed of 0.01"/min., and the measured values taken at a 5% secant line according to ASTM standards.

Rising-load K_{Iscc} tests were conducted in the 3-point bend configuration with a small corrosion cell attached to the V-notch containing a 3.5% aqueous solution of sodium chloride. The crosshead speed of 0.0002"/min. gave a stress-intensity rate increase of approximately 0.9 ksi$(in)^{1/2}$/min., which is within the recommended limit given by ASTM-STP 610 (28) (there are no ASTM standards for this test). The exposure was prolonged further by an initial incubation period of 1 hour at a stress intensity of 5 ksi$(in)^{1/2}$, followed by alternate rising load and 1 hour holding at increments of 5 ksi$(in)^{1/2}$ during which time the solution was replaced. The 1 hour holding period was introduced to increase the severity of the test. Constant-load long-time K_{Iscc} specimens were tested in a cantilever beam fixture in contact with a 3.5% sodium chloride aqueous solution which was changed daily. This test was carried out to establish a true minimum K_{Iscc} value. The constant-load tests were performed at the Army Materials Technology Laboratory, Watertown, MA.

Microscopy

The general martensitic microstructure was clearly revealed using a nital or picral etch. Etching for grain-size measurements was accomplished with a solution of 10 g picric acid and 4 g sodium tridecylbenzene sulfonate in 200 ml water. The solution was heated to 60°C and continuously stirred. Samples were swabbed for several minutes until the desired structure was achieved, often requiring repolishing. The ASTM E112 linear intercept technique was used for grain-size measurements.

Thin foils of the HIP'ed bar were prepared for STEM analysis by the following procedure: samples 0.8 mm thick were sliced from a 1 cm diameter bar using a diamond saw and ground by hand to approximately 0.13 mm; 3 mm diameter discs were punched and grinding was continued by hand with 600 grit SiC paper until the specimens were approximately 0.09 mm thick. The discs were then chemically thinned by jet polishing using a solution of 10% perchloric acid (40 ml) and 90% high-purity methanol (360 ml) at a bath temperature of less than -35°C. Particles were analyzed on a VG HB5 STEM by the x-ray energy dispersive analyzer equiped with a windowless detector allowing light-element analysis. AMR 1000 scanning electron microscope fractographs were taken of the tensile, K_{Ic}, and K_{Iscc} fracture surfaces, and conventional EDAX was used for chemical analysis.

RESULTS AND DISCUSSION

Processing

The experiments conducted at Pratt and Whitney originally were to consist of two 15 kg (33 lb.) heats, the first with a 0.15% addition of lanthanum as $LaNi_5$, and the second with a 0.05% addition. During the processing of both heats, the nozzles froze off prematurely preventing complete atomization of the melt. The metal remaining in the crucible of heat 1 was then reprocessed with no additional lanthanum added. The powder from these three heats was poor in quality with irregular shaped particles, some of which obviously were not

rapidly solidified. The size distribution used for consolidation was 2% -325 mesh (45.5 um), 10% -270 mesh (54.8 um), and 88% -80 mesh (185 um) including the irregular particles. Chemical analysis and examination of the microstructure revealed cross contamination by Fe-Ni powder particles and high-phosphorus steel particles from previous runs. For the most part, the cross contamination remained undissolved in the matrix, resulting in isolated regions of contamination. The combination of particulate and chemical contamination was most severe in RSP heat 1 (0.06% La) and the general cleanliness improved in heats 2 (0.025% La) and 3 (0.01% La). Although the lanthanum recoveries were consistent with prediction, the excessive phosphorus concentration was not anticipated and as a result, there was insufficient lanthanum to getter all the phosphorus. Fortunately, the high-phosphorus steel powder did not completely dissolve and regions of high phosphorus are believed to be localized.

Structure

Grain-coarsening behavior is summarized in Figure 2 for both the HIP'ed and extruded material,

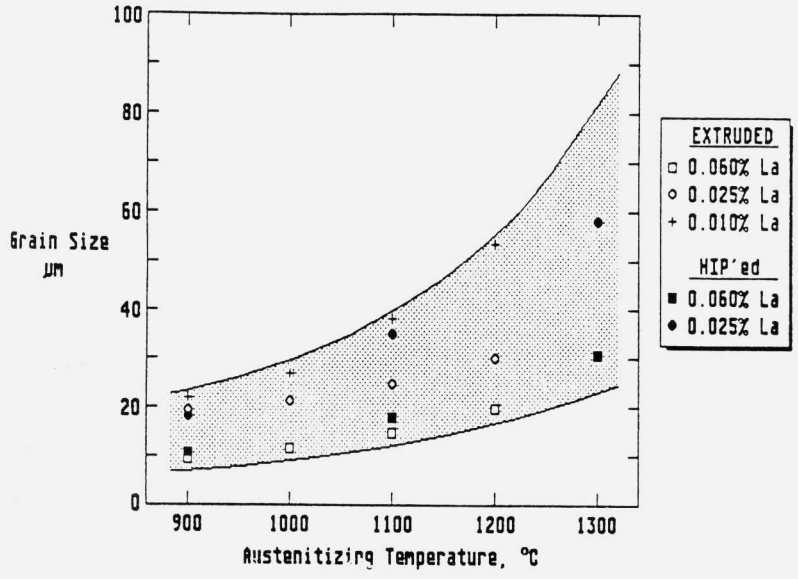

Figure 2. Ni-Mo-La steel grain-coarsening resistance; grain size vs. austenitizing temperature (1 hour) for extruded and HIP'ed samples.

where grain diameter in μm is plotted vs. austenitizing temperature from 900°C to 1300°C. Trends with lanthanum concentration reflect the variation in second-phase volume fraction. The 0.06% lanthanum heats exhibit excellent coarsening resistance, even at 1300°C. The low-lanthanum heat also provides good resistance to coarsening up to 1200°C. This behavior attests to the very high stability of the second-phase particles which are pinning the grain boundaries.

STEM analysis of precipitates in the consolidated material revealed three types of particles smaller than 0.1 μm in diameter. The smallest group consists of particles thought to originate from melt/crucible reactions and are La-Al-O ($LaAlO_3$) and Al-O (Al_2O_3). The second group shown in Figure 3 represents examples of the desired sulfur-containing precipitates and a corresponding X-ray spectrograph. The cluster of oxysulfide

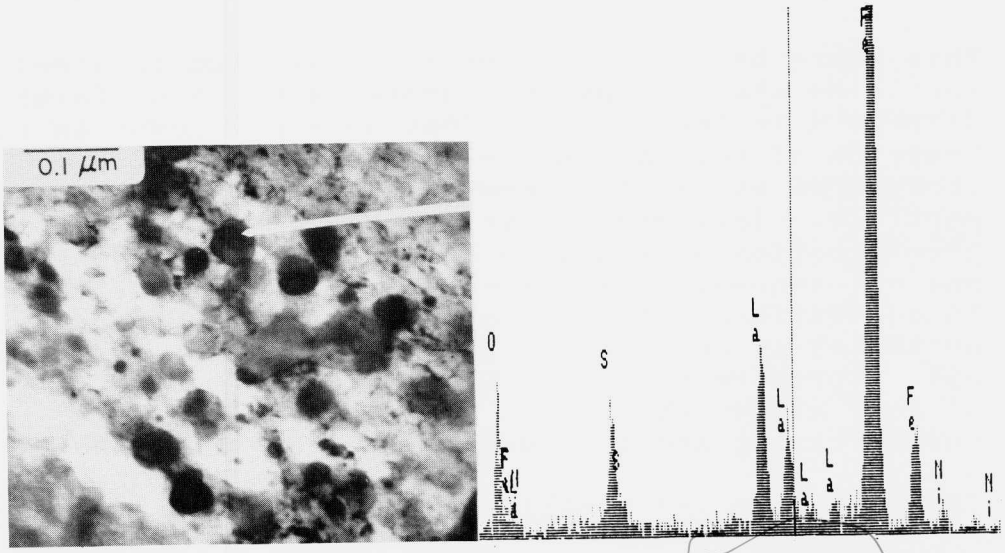

Figure 3. STEM micrograph of La-O-S (La_2O_2S) precipitates and a typical X-ray spectrograph.

precipitates is not typical, but illustrates the size distribution obtained which ranges from 100 Å to 800 Å. The third group, and most significant, are the La-O-P precipitates believed to

be $LaPO_4$. Figure 4 shows a typical particle with corresponding X-ray spectrograph.

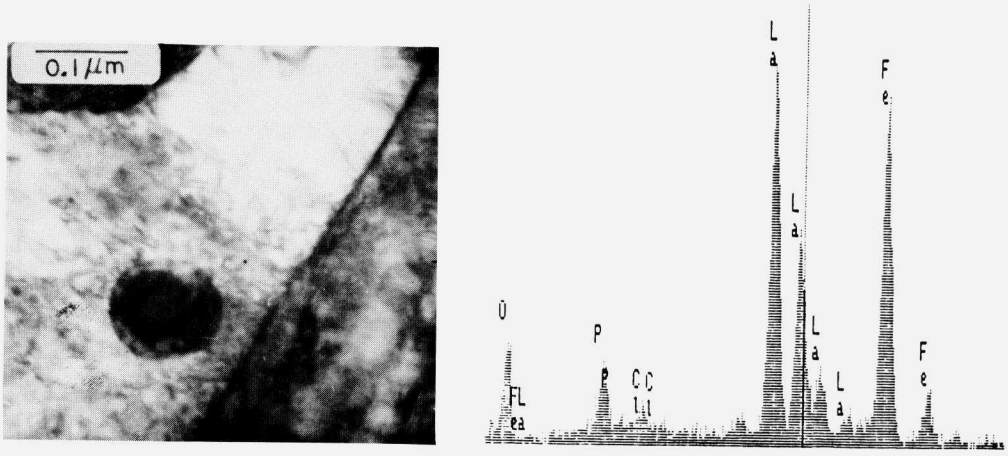

Figure 4. STEM micrograph of La-O-P ($LaPO_4$) precipitate and corresponding X-ray spectrograph.

This phase has never before been reported in steel. Particles are <0.1 μm in diameter and are uniformly dispersed in the matrix. Just as significant as the creation of this new phase is the fact that phosphorus and sulfur were not observed in the same particle. This means that the $LaPO_4$ and La_2O_2S precipitation events were completely independent, and not sequential as previously reported (8,9,24), in conventional steel processing where phosphorus nucleates as Fe_3P on oxysulfide particles, or not at all. Furthermore, the low thermodynamic stability of Fe_3P allows phosphorus to dissolve during austenitizing and this does not occur with $LaPO_4$.

Thermodynamic and Kinetic Models

The selection of a gettering agent was based primarily on the solution thermodynamic properties of compounds in the Fe-La-O-P and Fe-La-O-S systems. The two phases selected as the most stable compounds of phosphorus and sulfur were $LaPO_4$ and La_2O_2S. The experimental results indicate that these phases, or at least phases of very similar composition, have in fact been produced for the first time by late additions of lanthanum and RSP. To further

understand the role that these precipitates play in phosphorus and sulfur gettering, phase stability and classical nucleation models have been developed and are presented in the following section. All the phase stability calculations are based on Henrian activity given by:

$$h_i = (wt.\%i)(f_i) \tag{2}$$

where wt.%i is the composition of species i in weight % under the given conditions, and f_i is the Henrian activity coefficient of i.

Construction of the Fe-La-O-S phase stability diagrams are based on the following equations:

$$2\underline{La}(\%)+3\underline{O}(\%)=La_2O_3(s) \tag{3a}$$
$$h_O=(h_{La}{}^2K_3)^{-1/3} \tag{3b}$$

$$\underline{La}(\%)+\underline{S}(\%)=LaS(s) \tag{4a}$$
$$h_S=(h_{La}K_4)^{-1} \tag{4b}$$

$$2\underline{La}(\%)+2\underline{O}(\%)+\underline{S}(\%)=La_2O_2S(s) \tag{5a}$$
$$h_S=(h_{La}{}^2h_O{}^2K_5)^{-1} \tag{5b}$$

$$LaS(s)+\underline{La}(\%)+3\underline{O}(\%)=La_2O_3(s)+\underline{S}(\%) \tag{6a}$$
$$h_S=h_{La}h_O{}^3K_6 \tag{6b}$$

$$La_2O_2S(s)+\underline{O}(\%)=La_2O_3(s)+\underline{S}(\%) \tag{7a}$$
$$h_S=h_OK_7 \tag{7b}$$

$$LaS(s)+\underline{La}(\%)+2\underline{O}(\%)=La_2O_2S(s) \tag{8a}$$
$$h_O=(h_{La}K_8)^{-1/2} \tag{8b}$$

where

$$K_i=\exp(-\Delta G_i/(RT)) \tag{9}$$

Elements expressed as $\underline{i}(\%)$ are in solution and (s) represents the bulk solid compound. Equations 3, 4, and 5 represent the equilibria between the bulk compound and the elements in solution in liquid iron. Equations 6, 7, and 8 are the equilibria between the two bulk phases and the corresponding elements in solution in liquid iron, and are the sum

of equations 3+(-4), 3+(-5), and 5+(-4), respectively. Figure 5 is a schematic representation of the combined solubility surface for equations 3(La_2O_3), 4(LaS), and 5(La_2O_2S). The intersections of these surfaces are defined by equations 6, 7, and 8.

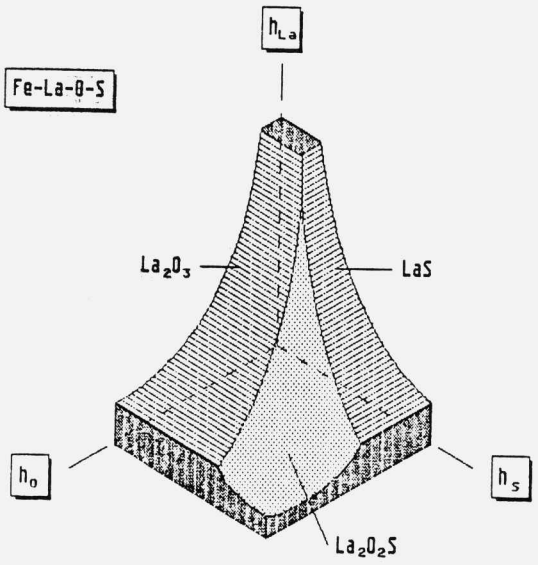

Figure 5. Schematic representation of the solubility surface in the Fe-La-O-S system at a given temperature in the range of interest.

Construction of the Fe-La-O-P phase stability diagrams are based on the following equations:

$$\underline{La}(\%)+\underline{P}(\%)=LaP(s) \quad (10a)$$
$$h_P=(h_{La}K_{10})^{-1} \quad (10b)$$

$$\underline{La}(\%)+\underline{P}(\%)+4\underline{O}(\%)=LaPO_4(s) \quad (11a)$$
$$h_P=(h_{La}h_O{}^4K_{11})^{-1} \quad (11b)$$

$$LaP(s)+\underline{La}(\%)+3\underline{O}(\%)=\underline{P}(\%)+La_2O_3(s) \quad (12a)$$
$$h_P=h_{La}h_O{}^3K_{12} \quad (12b)$$

$$LaPO_4(s)+\underline{La}(\%)=\underline{P}(\%)+\underline{O}(\%)+La_2O_3(s) \quad (13a)$$
$$h_P=h_{La}K_{13}/h_O \quad (13b)$$

$$LaP(s)+4\underline{O}(\%)=LaPO_4(s) \quad (14a)$$
$$h_O=K_{14}^{-1/4} \quad (14b)$$

Equations 3, 10, and 11 represent the equilibrium between the bulk compound and the elements in solution in liquid iron. Equations 12, 13, and 14 are the equilibria between the two bulk phases and the corresponding elements in solution in liquid iron, and are the sum of equations 3+(-10), 3+(-11), and 11+(-10), respectively. Figure 6 is a schematic representation (6a for T≥1475°C and 6b for T<1475°C) of the combined solubility surfaces for equations 3(La_2O_3), 10(LaP <1475°C), and 11($LaPO_4$). The intersections of these surfaces are defined by equations 12, 13, and 14.

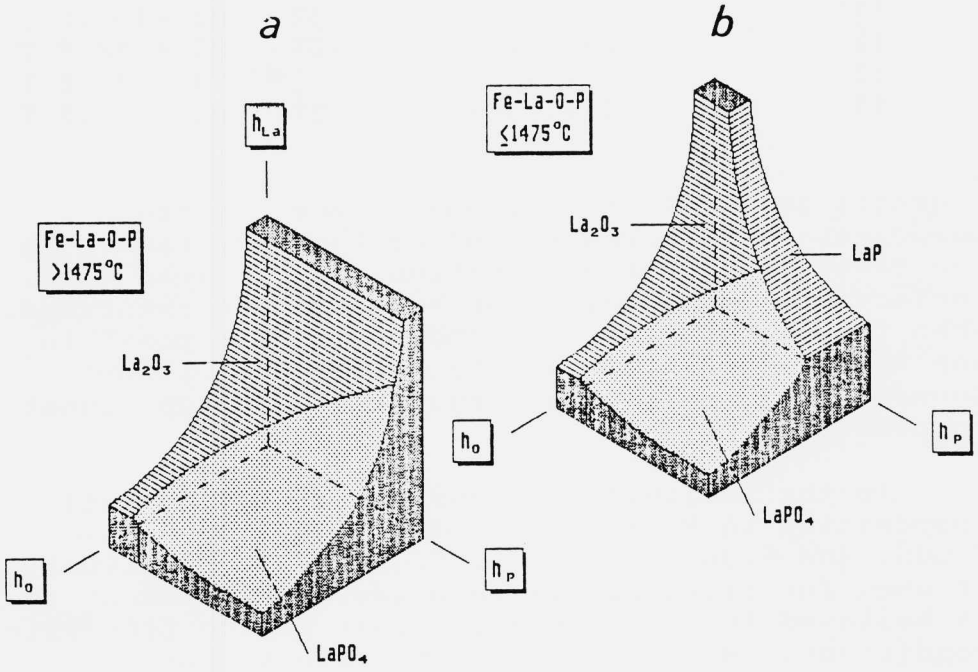

Figure 6. Schematic representation of the solubility surface in the Fe-La-O-P system; a) >1475°C, b) ≤ 1475°C.

Table 3 (21-27) lists the free energy of formation from liquid iron used in equation 9 to calculate the chemical equilibrium constant K_i for reaction equations 3-14. Figures 5 and 6 represent

the phase stability surfaces at constant temperature that are of interest in this study. A composition (activity) that lies below this surface has all

TABLE 3

Free Energy of Formation from Liquid Iron for the Fe-La-O-S and Fe-La-O-P Systems

Equation No.	Compound	Free Energy, cal/mol
3	La_2O_3	-344 865 + 80.5 T
4	LaS	- 91 750 + 25.5 T
5	La_2O_2S	-320 340 + 71.9 T
6	3+(-4)	-253 115 + 55.0 T
7	3+(-5)	- 24 525 + 8.6 T
8	5+(-4)	-228 590 + 46.4 T
10	LaP	- 55 580 + 31.8 T
11	$LaPO_4$	-327 282 +105.0 T
12	3+(-10)	-289 285 + 48.7 T
13	3+(-11)	- 17 583 - 24.5 T
14	11+(-10)	-271 702 + 73.2 T

elements in solution. If one or more of the components are increased and/or the temperature is decreased, the bulk composition moves beyond this surface and the liquid iron becomes supersaturated. When this occurs it is thermodynamically possible for the appropriate phase to exist, but without knowledge of kinetic factors, precipitation cannot be predicted.

In the following discussion, a hypothetical composition in Henrian activity of 0.1, 0.001, 0.005, and 0.005 for La, O, S, and P, respectively, is used for illustrative purposes. This composition is believed to be reasonably close to the processing conditions. However, since the interaction coefficient for lanthanum is uncertain, only a rough approximation of wt.% can be made for La, P and S. Therefore, all calculations are performed in terms of Henrian activity.

A calculated Fe-La-O-S phase stability diagram is plotted in Figure 7 as h_S vs. h_O at constant h_{La} (0.1) and decreasing temperature from 1650°C. The composition at point A is just inside the La_2O_3

phase field where La_2O_2S is metastable. With decreasing temperature, the equilibrium line between La_2O_3 and La_2O_2S shifts to lower oxygen and higher sulfur activity favoring the oxide phase. This diagram indicates that at 1650°C La_2O_3 is stable in the melt, but with a small degree of deoxidation, La_2O_2S becomes stable, and this condition will prevail with a decrease in melt temperature.

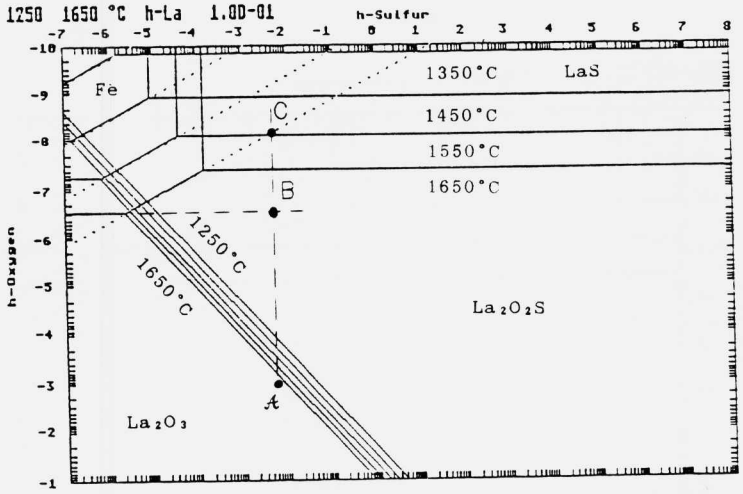

Figure 7. Phase stability diagram of S vs. O, in Henrian activities, at constant La and decreasing temperature.

A calculated Fe-La-O-P phase stability diagram is plotted in Figure 8 as h_P vs. h_O at constant h_{La} (0.1) and decreasing temperature from 1650°C. Metastable phases are shown in parenthesis and the dotted line denotes the metastable equilibrium between liquid iron and $LaPO_4$. The stable phase is La_2O_3 at point A which is just above the metastable phase field of $LaPO_4$ at 1650°C. With decreasing temperature, a significant movement of the metastable $LaPO_4$ phase field is indicated. The LaP phase field can be seen appearing at 1450°C in this diagram. Analysis of the Fe-La-O-P system at 1650°C indicates that La_2O_3 is the only solid phase that can exist until the temperature is lowered to

approximately 1600°C at which point the metastable $LaPO_4$ phase is possible.

A summary of the possible phases that might exist in the melt at 1650°C at the hypothetical composition includes the stable phase La_2O_3 and the metastable phase La_2O_2S. With decreasing temperature, the additional metastable phase $LaPO_4$ is possible. This thermodynamic analysis indicates what phases might be present under metastable conditions, but does not predict their nucleation.

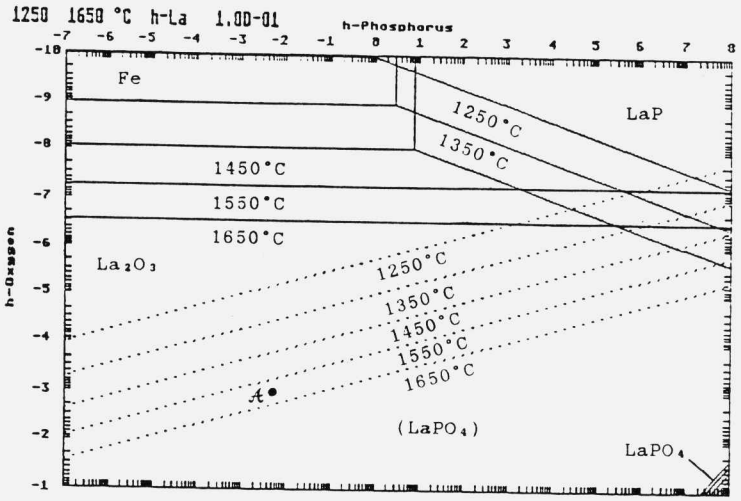

Figure 8. Phase stability diagram of P vs. O, in Henrian activities, at constant La and decreasing temperature.

The following discussion is concerned with supersaturation in liquid iron before solidification begins and does not include solute rejection during solidification. Under slow cooling, supersaturations gradually build up in the liquid until sufficient driving force is reached for nucleation. Following this scenario, the first phase to reach this critical supersaturation is presumed to precipitate, followed sequentially by the other phases provided they are thermodynamically stable and the first phase does not deplete the concentration to prevent critical supersaturation.

During rapid solidification processing, when the liquid is rapidly supercooled, but before solidification begins, critical supersaturation levels for oxygen are likely to occur for oxysulfide and phosphate compounds simultaneously. The supersaturation of oxygen with respect to the oxide and oxysulfide compounds based on the hypothetical composition of La and S is shown in Figure 7. Points B and C represent the equilibrium oxygen composition at 1650°C for La_2O_3 and La_2O_2S, respectively. The difference A-B and A-C represents the relative amount of supersaturation. Assuming all other conditions are equal between the two phases, La_2O_2S has the greatest driving force to nucleate, although the equilibrium diagram indicates La_2O_3 as the stable phase. Furthermore, the driving force increases significantly with decreasing temperature.

A modified version of the classical nucleation model by Turpin and Elliott (29) was adapted to calculate the oxygen supersaturation ratio, minimum critical interfacial energy required for nucleation, and nucleation temperature. The parameters that are specified include melt temperature, equilibrium oxygen, melt oxygen, and for the compound, molar volume, enthalpy, and interfacial energy, if known. From this analysis, a rough idea of the kinetics of the melt can be determined after late additions of lanthanum. Data from the hypothetical composition and melt temperature of 1650°C were used for La_2O_3, La_2O_2S, and $LaPO_4$ with the respective equilibrium oxygen values from the phase stability diagram of 2.8×10^{-7}, 6.0×10^{-9}, and 1.7×10^{-3}. The estimated interfacial energy for all three compounds was taken as 1.5 J/m^2 which represents the midpoint of a range of reported values. Assuming the same interfacial energy, and a nucleation rate of $1/cm^3/s$, La_2O_3, La_2O_2S, and $LaPO_4$ have homogeneous nucleation temperatures of 1842°C, 2059°C, and 1171°C, respectively, indicating that the oxide and oxysulfide should spontaneously nucleate in the melt, and that the phosphate will require significant supercooling to nucleate. The minimum critical interfacial energy required for nucleation at the melt temperature was calculated for the oxide and oxysulfide. The interfacial energy for La_2O_3 must be less than 1.79 J/m^2 for homogeneous nucleation to occur at 1650°C; likewise, the

interfacial energy for La_2O_2S must be less than 2.33 J/m^2. Although the actual interfacial energy values are unknown for these compounds, it is not unreasonable to predict that La_2O_2S has a greater driving force for nucleation than La_2O_3. The results for $LaPO_4$ indicate that if a high degree of supercooling can be reached before nucleation of the oxide and oxysulfide occurs, sufficient oxygen supersaturation in the melt will exist to promote nucleation of this phase.

The cooling rate of the liquid from the superheat to the atomization temperature is equally as important as rapid solidification. The thermodynamic and kinetic models suggest that through rapid cooling of the liquid and RSP, the independent precipitation of $LaPO_4$ and La_2O_2S is possible, whereas via conventional processing only coarse La_2O_3 and La_2O_2S precipitates would form, preventing the melt from reaching sufficient oxygen supersaturation to nucleate $LaPO_4$. This explains why the latter phase has not been observed before. Future designs in atomizing and melt-spinning units for application of this alloy/process system need to address the cooling rate in the liquid before solidification. Ideally, atomization should take place at the superheat temperature.

The experimental results indicate a new La-O-P ($LaPO_4$) phase has been created and a known phase, La-O-S (La_2O_2S) has been produced in a much finer dispersion than previously reported. Both of these phases exhibit remarkable coarsening resistance. After a total of three hours at 1100°C there was essentially no measurable coarsening above 0.1 um. This is consistent with the high thermodynamic stability of these compounds. Comparing these results with Hsu's (19) observations on RSP matrix tool steels, the lanthanum phases have a smaller particle diameter by nearly one order of magnitude and exhibit greater coarsening resistance after more severe thermal treatments.

Properties

Hardenability was not explicitly determined because of the lack of material to produce Jominy test specimens; however, examinations of small sections cooled at known cooling rates compared with

the continuous cooling transformation diagram of 4340 indicates that the hardenability was comparable. Also, through hardness was achieved in bars of 15 mm (0.591 in) diameter.

The hardness response to heat treatment is summarized for the extruded material in Figure 9 comparing the three lanthanum levels for 1100°C austenitizing. In each case, there is excellent response to tempering temperature, and the 1100°C austenitizing temperature provides the desired hardness at a 200°C temper. Differences in the three heats correspond to carbon variations.

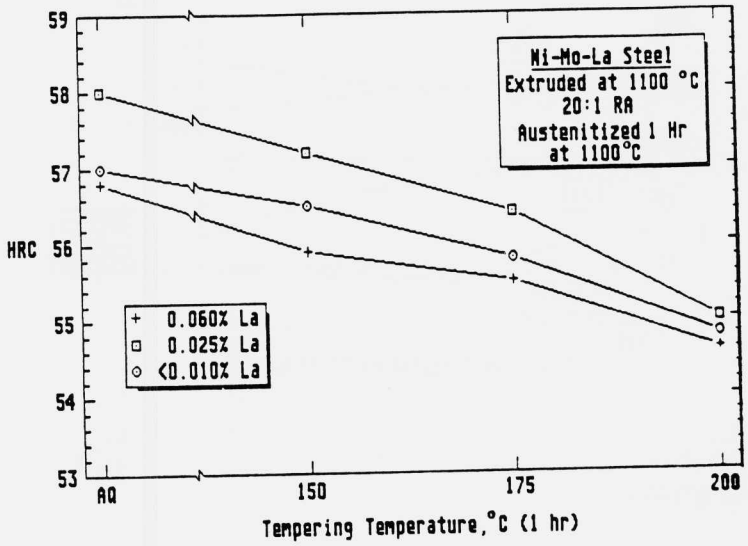

Figure 9. Hardness response for RSP heats 1, 2, and 3. HRC vs. tempering temperature, austenitized 1 hour at 1100°C.

Results of the tensile tests for the 0.06% and 0.025% lanthanum heats are given in Figure 10. Tensile specimens were not made for the 0.01% heat due to a shortage of material. Excellent yield strengths of 1718-1863 MPa (249-270 ksi) and ultimate strengths of 2091-2456 MPa (303-356 ksi) were achieved over the tempering temperature range. The reduction in area suffered due to the cross contamination present, particularly in the high-

lanthanum heats. The total elongation is given in Figure 10 and, along with the uniform elongation which was approximately 10% less, represents good behavior at these strength levels. The 0.06% specimen tempered at 175°C failed at the onset of necking due to a large inclusion.

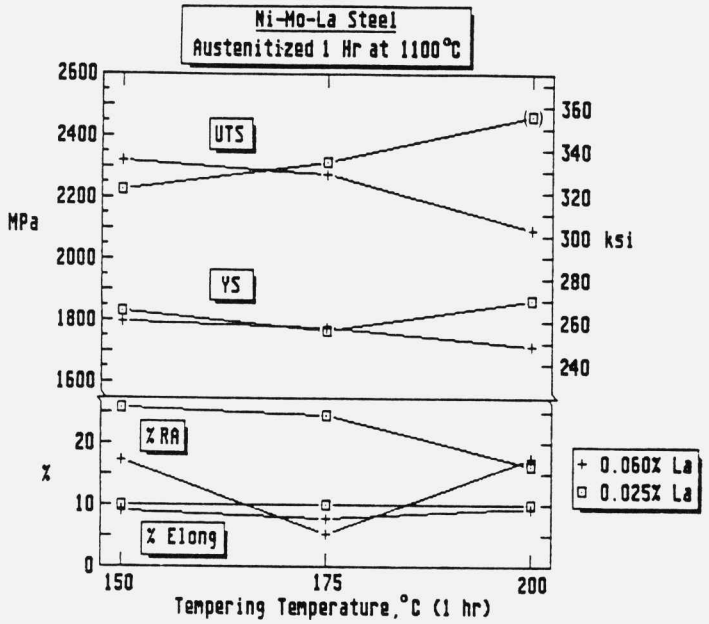

Figure 10. Combined tensile properties for Ni-Mo-La steel, RSP heats 1 and 2. UTS, YS, %RA, and %Elong vs. temperature.

The SEM fractograph of the tensile specimen shown in Figure 11a is typical of all samples tested. In all but one case, fracture initiated on the surface at a large inclusion or Fe-Ni powder particle. Figure 11b shows the remains of an imbedded Fe-Ni particle at the initial point of fracture. In the instance where failure did not occur at the surface, it originated in a region of gross contamination. Figure 12a illustrates an undissolved Fe-Ni powder particle on the fractured surface. The fracture mode was clearly dimple rupture with void coalescence, as exhibited in Figure 12b. The particles present in the dimples were analyzed by EDAX to contain lanthanum, but no

sulfur or phosphorus was detectable. Inspite of the serious powder cross contamination present, the tensile properties of this material are quite good.

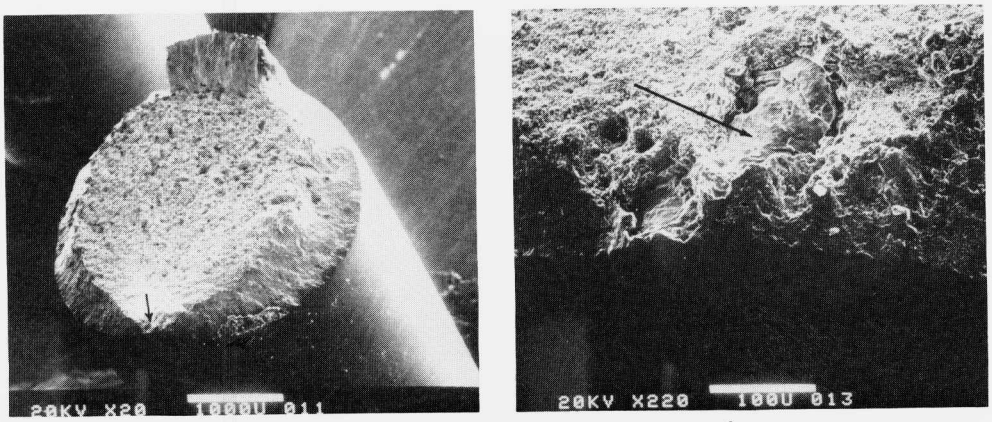

Figure 11. SEM micrographs of Ni-Mo-La steel fractured tensile bar; a) fractured surface, b) Fe-Ni particle at fracture initiation point.

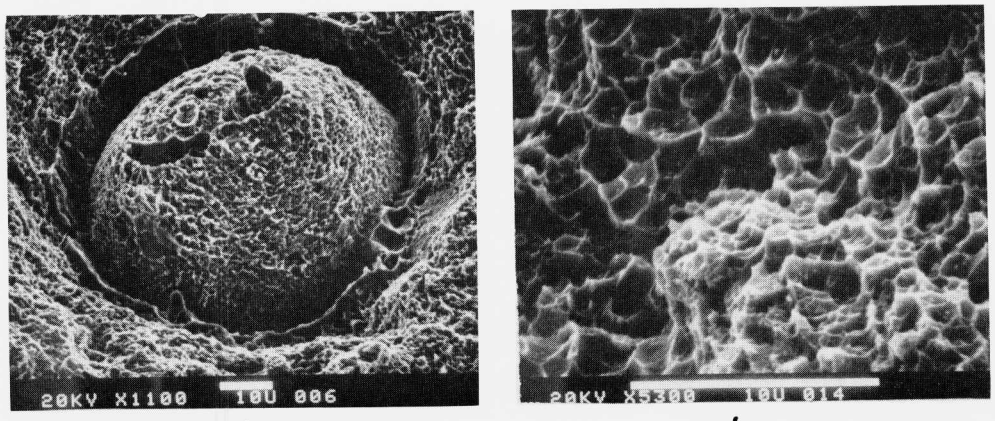

Figure 12. SEM micrographs of Ni-Mo-La steel fractured tensile bar; a) Fe-Ni particle, b) typical dimple ruptured fracture.

The sharp-crack fracture toughness results likewise suffered from the contamination, with low readings for the dirtiest material and excellent readings for the cleanest heat. The fracture surface for RSP heat 1 is shown in Figure 13.

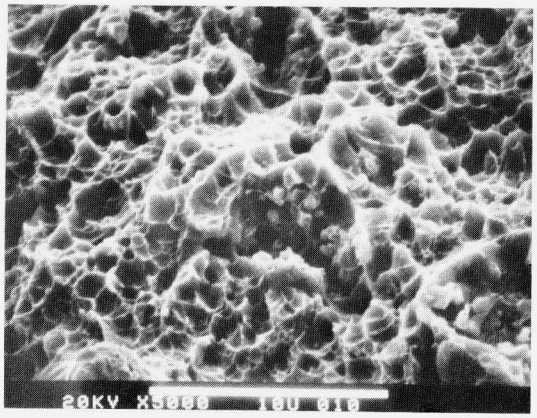

Figure 13. SEM micrograph of Ni-Mo-La steel fractured K_{Ic} specimen, RSP heat 1 at 5000X.

The corresponding stress-intensity values measured for heats 1, 2, and 3 are 33-41 MPa(m)$^{1/2}$ (30-37 ksi(in)$^{1/2}$), 44-51 MPa(m)$^{1/2}$ (40-46 ksi(in)$^{1/2}$), and 59-67 MPa(m)$^{1/2}$ (54-61 ksi(in)$^{1/2}$), respectively. The mode of fracture in the sharp-crack specimens appears to be 100% ductile discounting obvious areas of contamination. This differs remarkably from 4340, which typically exhibits partial quasi-cleavage at these strength levels. At the center of Figure 13 a typical area of contamination is visible, contributing to the low toughness in heats 1 and 2.

Figure 14 compares a schematic cross section of the four rising-load K_{Iscc} test specimens. In the case of the 0.06% and 0.025% lanthanum heats, the extrusion can is contained in the sample. It was necessary to use a heavy-walled container to make up for an insufficient amount of powder for the extrusion process in heats 1 and 2. Consequently, a smaller diameter consolidated area was produced and a portion of the can material had to be included in the test specimen. The presence of the can material

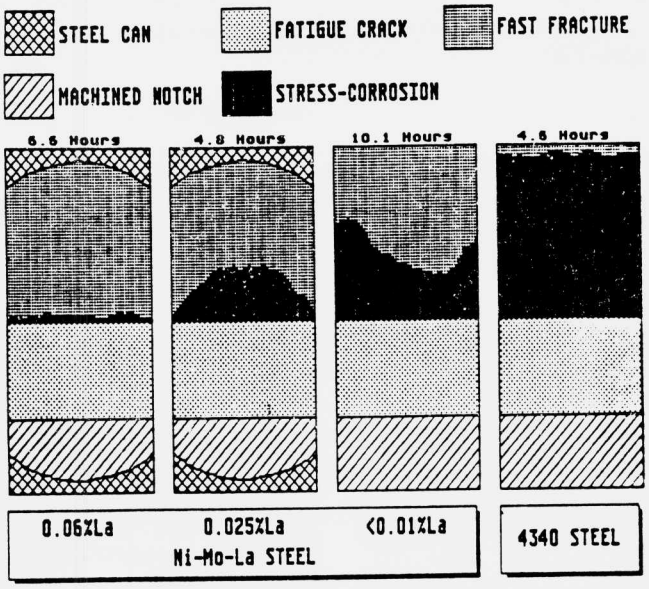

Figure 14. Schematic representation of corrosion attack on K_{Iscc} specimens of Ni-Mo-La and 4340 steel.

has undoubtedly affected the stress at the crack tip, resulting in premature mechanical failure and not corrosion failure. The 0.01% lanthanum sample was free of any can material and may be compared directly with the 4340. On a qualitative basis, looking at the four samples, there is a significant decrease in the region of attack with increasing lanthanum. Realizing that in the 0.06% and 0.025% cases the stresses were probably higher, it appears the lanthanum has been effective, particularly when comparing the time of exposure. Assuming that the loading was similar in intensity at the crack tip, and comparing the first two specimens, the longer exposure has significantly less attack with the higher lanthanum.

Figure 15 compares RSP heat 3 with the VAR 4340 at the same hardness, and demonstrates a dramatic difference in the mode of fracture, moving away from pure intergranular fracture with increasing lanthanum concentration. The stress-corrosion

stress intensities for heat 3 and 4340 are 40.8 MPa(m)$^{1/2}$ (37.1 ksi(in)$^{1/2}$) and 11.2 MPa(m)$^{1/2}$ (10.2 ksi(in)$^{1/2}$), respectively, indicating a substantial improvement for the first time in the resistance to stress-corrosion failure in ultrahigh-strength steels.

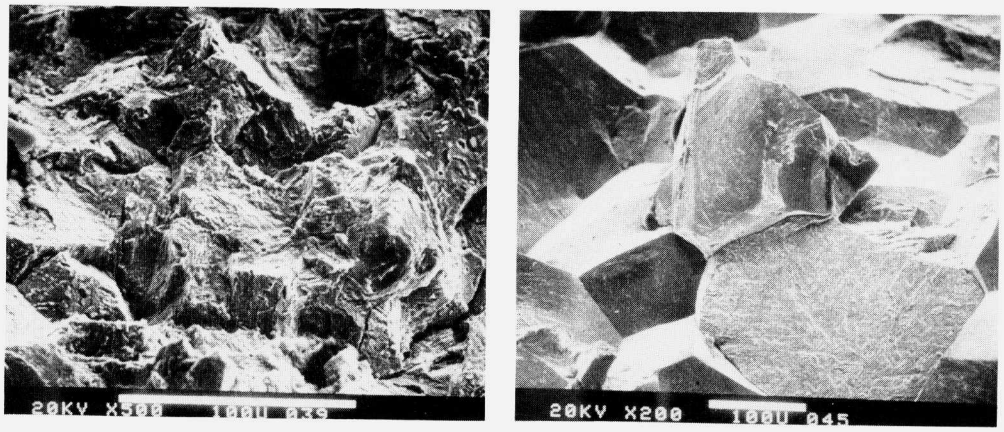

a *b*

Figure 15. SEM micrographs of K_{Iscc} fractured surfaces, a) RSP Ni-Mo-La steel heat 3, and b) 4340 steel.

A summary of the K_{Ic} and the K_{Iscc} results for the Ni-Mo-La steels and VAR/ESR 4340 is given in Figure 16. In the high-lanthanum heat, with good gettering but poor fracture toughness, the K_{Iscc} approaches K_{Ic}. With improved cleanliness and less effective gettering, the K_{Ic} improves with a reduction of K_{Iscc}. Due to the presence of the can material in samples from heats 1 and 2, they cannot be quantitatively compared with heat 3 and the 4340 samples. Heat 3 represents the cleanest case, and at 0.01% La, has the least gettering effect while the fracture toughness and resistance to stress-corrosion is the highest. This implies that the base material itself has good stress-corrosion resistance. These values are compared with typical VAR and ESR 4340 heats showing a significant improvement for the same hardness. The solid lines in the figure on the 4340 bars denote the range of handbook data for this hardness level.

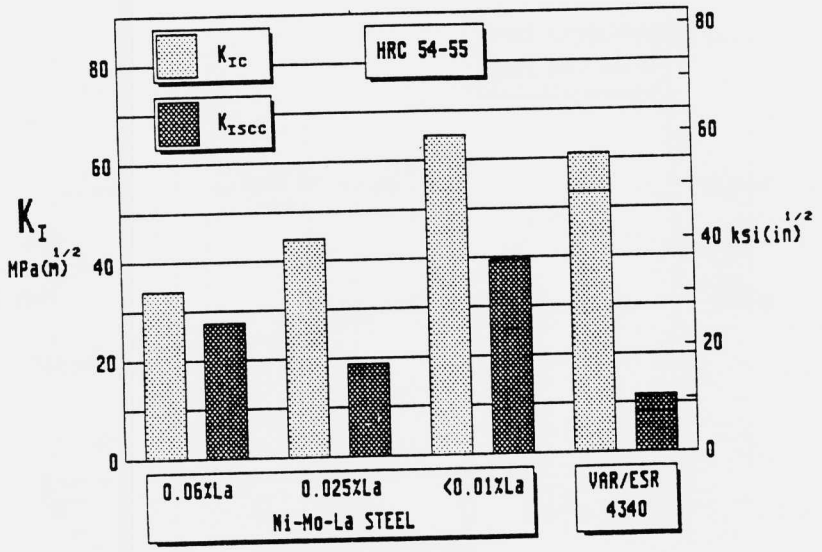

Figure 16. Comparison of K_{Ic} and K_{Iscc} for Ni-Mo-La steel (heats 1, 2, and 3) and VAR/ESR 4340 at HRC 54-55.

Long-time constant load K_{Iscc} tests were conducted on three samples, one at each level of lanthanum, and these results are shown in Figure 17 compared with available ESR 4340 data (30). The high and medium lanthanum samples (heats 1 and 2) failed at 2 hours and 35 hours, respectively, and the low lanthanum specimen (heat 3) survived the required 1000 hours to establish an official K_{Iscc} value. All specimens were loaded to an initial 22 MPa(m)$^{1/2}$ (20 ksi(in)$^{1/2}$) and, in spite of the significant amounts of can material and severe contamination near the can/sample interface, heats 1 and 2 displayed greater resistance to corrosion by surviving longer than the 4340 at the same initial load. The cleanest specimen from heat 3 at 0.01% lanthanum survived 1000 hours at 20 ksi(in)$^{1/2}$ representing at least a 100% improvement over 4340. Examination of this specimen after 1000 hours indicated that no measurable crack growth had occurred. The extent to which the presence of the extrusion can in the cross section of samples from heats 1 and 2 has affected the stress-intensities

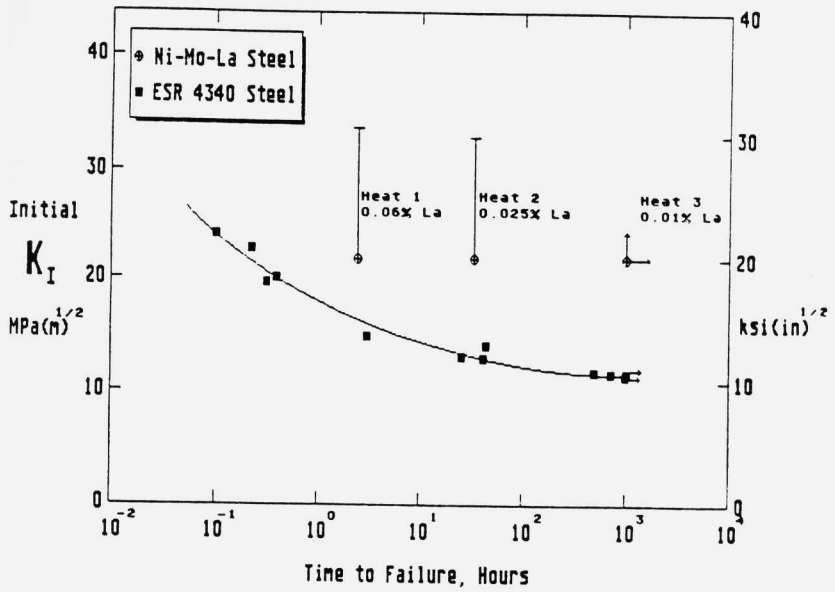

Figure 17. Initial stress-intensity factor vs. time to failure for ESR 4340 and Ni-Mo-La steel (30).

measurements is uncertain. The existence of a region of relatively weak can material which was included in the width dimension for stress-intensity calculations is believed to have resulted in some degree of higher loading on the crack tip. Calculating a new stress-intensity value for heats 1 and 2 without taking into account the can material results in a stress-intensity loading during the constant load test of 34 MPa(m)$^{1/2}$ (31 ksi(in)$^{1/2}$) and 33 MPa(m)$^{1/2}$ (30 ksi(in)$^{1/2}$), respectively. These values are represented in Figure 17 as upper limits to the corresponding data points for heats 1 and 2.

Summary

For the first time, highly stable fine dispersions of $LaPO_4$ and La_2O_2S have been produced in a novel RSP steel by late additions of lanthanum with the result of improved resistance to intergranular stress-corrosion cracking. Excellent yield and tensile strengths have been achieved with

superior fracture toughness to 4340 at the same hardness level. The fracture mode was 100% ductile in contrast to partial quasi-cleavage typical in 4340. Rising-load and constant-load K_{Iscc} results are superior to 4340 by a factor of 2-4, representing an exceptional advancement in stress-corrosion resistance at HRC 55. A significant shift away from the intergranular mode of stress-corrosion fracture typical of 4340 occurs with increasing lanthanum, as well as a reduction in the total area of attack.

An analysis of simple thermodynamic and kinetic models indicates that high supersaturations of oxygen are required to produce $LaPO_4$, and this becomes possible through rapid cooling of the liquid and RSP. Finally, Figure 18 presents a comparison of three high-strength steels (31) and the Ni-Mo-La steel in a plot of K_{Iscc} vs. ultimate tensile strength emphasizing the potential engineering importance of this novel Ni-Mo-La steel alloy.

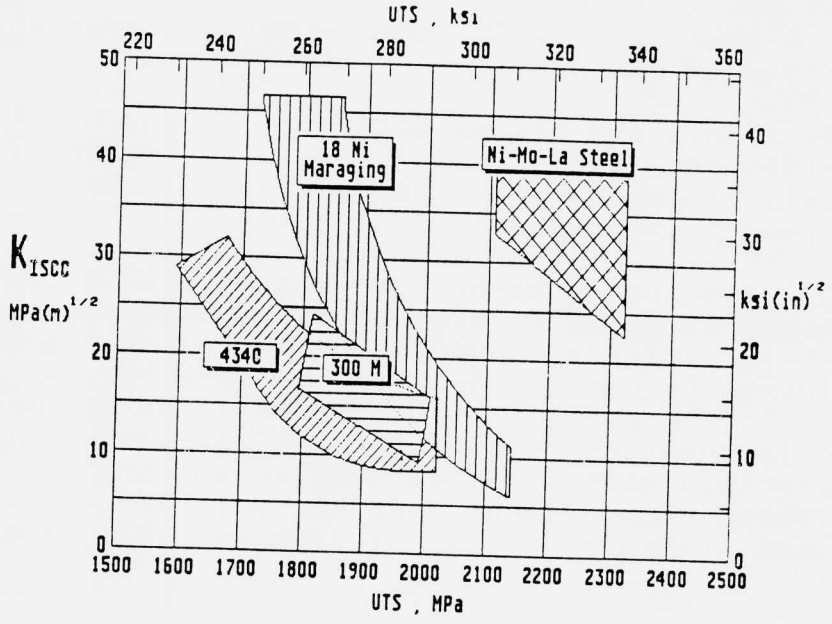

Figure 18. Comparison of K_{Iscc} vs. UTS for 3 high strength steels and the Ni-Mo-La steel (31).

Based on this work, two 136 kg (300 lb.) RSP heats of Ni-Mo-La steel have been produced at the Carpenter Technology Corporation and are currently under evaluation.

CONCLUSIONS

1. Gettering of phosphorus and sulfur was achieved for the first time by independent precipitation of La-O-P ($LaPO_4$) and La-O-S (La_2O_2S) after controlled late addition of $LaNi_5$ and rapid solidification processing.

2. Rapid cooling of the melt as well as RSP is essential to prevent early precipitation of La_2O_2S and La_2O_3 as coarse primary inclusions which would then deoxidize the melt below the critical level of oxygen supersaturation needed for nucleation of $LaPO_4$.

3. The second-phase dispersion remains small ($\leq$1000 Å) and provides effective grain-boundary pinning during consolidation at 1100°C and austenitizing to 1300°C. The oxysulfides range from 100 to 800 Å and the phosphates from 800 to 1000 Å after 3 hours at 1100°C, demonstrating remarkable coarsening resistance.

4. Yield and ultimate tensile strengths of 1718-1863 MPa (249-271 ksi) and 2091-2456 MPa (303-356 ksi), respectively, were achieved in spite of poor powder cleanliness.

5. Fracture toughness of heats 1 and 2 was seriously affected by cross contamination of Fe-Ni powder particles and exogenous inclusions. Heat 3, the lowest La and cleanest of the three heats, had a K_{Ic} of 65 $MPa(m)^{1/2}$ (59.2 $ksi(in)^{1/2}$) at 55 HRC which is superior to 4340 with the same hardness. The fracture mode was 100% ductile showing a significant improvement over the partial quasi-cleavage fracture typical of 4340 at these strength levels.

6. The stress-corrosion cracking resistance of the Ni-Mo-La RSP alloy exhibited at least a 100% improvement over 4340 with a constant-load K_{Iscc} of at least 22 $MPa(m)^{1/2}$ (20 $ksi(in)^{1/2}$). Rising-load

tests conducted on the same heat indicated a K_{Iscc} approaching 44 MPa$(m)^{1/2}$ (40 ksi$(in)^{1/2}$), representing a four-fold increase over 4340. Lanthanum additions produce a qualitative reduction in the extent of stress-corrosion attack and a significant shift away from the intergranular stress-corrosion fracture typical of 4340.

ACKNOWLEDGEMENTS

This research was supported by the National Bureau of Standards, Contract NB83NAHA4024, and in part by the Office of Naval Research, Contract N00014-81-K-0013. Starting billets for RSP were supplied by Republic/LTV Steel. We are grateful to Ms. Nancy Kackley of MTL for the constant-load K_{Iscc} testing.

REFERENCES

1. R.M.Latanision, O.H.Gastine, C.R.Compeau, Environment-Sensitive Fracture of Engineering Materials, Z.A.Foroulis, ed., Conf. Proc. TMS-AIME, 1977, p. 48.

2. N.Bandyopadhyay, Jun Kameda, and C.J.McMahon, Jr., Metall. Trans. Vol.14A, 1983, p. 881.

3. S.K.Banerji, C.J.McMahon Jr., and H.C.Feng, Metall. Trans. Vol.9A, 1978, p. 237.

4. D.Y.Lee, E.V.Barrera, J.P.Start, and H.L.Marcus, Metall. Trans. Vol. 15A, 1984, p. 1415.

5. M.P.Seah, Acta Metall.Vol 28, 1980, pp. 955-962.

6. M.P.Seah, P.J.Spencer, and E.D.Hondros, Metal Science, May 1979, p. 307.

7. M.Guttman, Surface Science, Vol.53, 1975, p. 213.

8. C.I.Garcia, G.A.Ratz, M.G.Burke and A.J.DeArdo, Journal of Metals, September 1985, p. 22.

9. P.E.Waudby, International Metals Reviews, No.2, 1978, p. 74.

10. C.Lea, Metal Science, March 1980, p. 107.

11. J.Kameda and C.J.McMahon Jr., Metall. Trans. Vol.12A, 1981, p. 31.

12. M.Guttmann, Ph.Dumoulin and M.Wayman, Metall. Trans. Vol. 13A, 1982, p. 1693.

13. N.Bandyopadhyay and C.L.Briant, Metall. Trans. Vol.14A, 1983, p. 2005.

14. B.D.Craig, Metall. Trans. Vol. 15A, 1984, p. 565.

15. J.Kameda and C.J.McMahon, Jr., Metall. Trans. Vol.13A, 1983, p. 903.

16. M.Suga, J.L.Goss, G.B.Olson, and J.B.Vander Sande, Proc. 2nd Int'l Conf. Rapid Solidification Processing: Principles and Technologies, Claitor's, Baton Rouge, 1980, p. 364.

17. P.M.Fleyshman, Fracture Toughness of Rapidly Solidified Martensitic Steels, M.S. Thesis, MIT, Cambridge, MA, Sept. 1982.

18. G.B.Olson, H.C.Ling, J.S.Montgomery, J.B.Vander Sande, and M.Cohen, Rapidly Solidified Amorphous and Crystalline Alloys, North-Holland, NY, 1982, p. 355.

19. Chen-Yih Hsu, Grain-Growth Mechanisms In Rapidly Solidified Matrix Steels, Ph.D. Thesis MIT, Cambridge, MA, February 1984.

20. J.F.Watton, Phosphorus Gettering in a Rapidly Solidified Ni-Mo-La Steel, Sc.D. Thesis, MIT, Cambridge, MA, June 1987.

21. J.A.N.A.F. Thermochemical Tables, 2nd ed., 1971.

22. O.Kubaschewski and C.B.Alcock, Metallurgical Thermochemistry, 5th ed., Pergamon, NY, 1979.

23. J.F.Elliott, M.Gleiser, and V.Ramakrishna, Thermochemistry for Steelmaking, Vols.I and II, Addison Wesley, MA, 1963.

24. W.G.Wilson, D.A.R.Kay, and A.Vahed, Journal of Metals, May 1974, p. 14.

25. G.K.Sigworth and J.F.Elliott, Metal Science, Vol. 8, 1974, p. 298.

26. C.H.P.Lupis, Chemical Thermodynamics of Materials, North-Holland, 1983.

27. N.Kippenhan, K.A.Gschneidner, Jr., Institute for Atomic Research, Iowa State University, IS-RIC-4, 1970 (Sponsored by MolyCorp.).

28. W.G.Clark, Jr. and J.D.Landers, ASTM STP 610, American Society for Testing and Materials, 1976, pp. 108-127.

29. M.L.Turpin and J.F.Elliott, Journal of the Iron and Steel Institute, March 1966, p.217.

30. G.B.Olson, A.A.Anctil, T.S.DeSisto, and E.B.Kula, Metall. Trans. Vol.14A, 1983, p. 1661.

31. R.J.Ault and G.W.Waid, Steel Research Group Newsletter #1, April 1985, MIT, Cambridge, MA.

Appendix

APPLICATION OF ARTIFICIAL INTELLIGENCE TO STEEL RESEARCH

RALPH J. HARRISON[1] AND INGEMAR A. HULTHAGE[2]
1) U.S. Army Materials Technology Laboratory, Watertown, MA 02172-0001; 2)The Robotics Institute, Carnegie-Mellon University, Pittsburgh, PA 15213.

INTRODUCTION

Our discussion of the application of Artificial Intelligence (AI) to steel research is not one which suggests that materials research scientists can be replaced by computer programs. We start from the premise that research is not simply an application of known techniques and rules to a problem, but it must also involve innovation and discovery. These are not yet things that one can do well by computer. But there are many research tools that are used to facilitate research and in trying to establish the usefulness of AI as one among many research tools we feel that we can define a realistic goal(1). In the present paper we describe our progress in designing a knowledge-based system for materials research. The technique used will be illustrated with regard to its potential application to the steel research program which has been described in other talks at this meeting.

In short, we have been trying to develop a system, a Knowledge Based System for Materials Research (KBMR) that will assist materials researchers in their pursuit of materials research and design goals. It differs from a traditional expert system which is designed to give a non-expert the benefit of expert knowledge. Rather it is to create a tool for the expert integrated with a knowledge medium for storing and communicating knowledge relevant to materials research. The KBMR will provide software tools to increase the productivity of the researcher in ways such as evaluating the status of the overall research plan: generating new design suggestions and performing some reasoning and calculations automatically in response to new facts or high level reasoning by the researcher. Through the utilization of AI techniques as well as conventional software, it is possible to go beyond algorithmic evaluation of data and assist the researcher with problem solving. The materials researcher engages in a mixed initiative dialog with the knowledge based system during which the user can both develop a particular design and add knowledge to the system for permanent storage.

HIGH STRENGTH STEEL RESEARCH

The Steel Research Group under NSF-MTL sponsorship has been applying a multi-prong approach to reach the goal of an improved high strength steel. The program involves many researchers specializing in experimental, theoretical, and phenomenological techniques. The KBMR could provide a medium for deposition and exchange of knowledge and data, including qualitative and quantitative models of relevant metallurgical mechanisms. It could also provide a tool for evaluating experimental data, generating model predictions, preparing and performing simulations and generating hypotheses.

There are features of the Steel Research which make it seem especially well suited for application of the KBMR. The chief of these is the fact that the research plan is well defined and given in detail, containing both the logic and the steps in the methodology. The initial plan formulated by Greg Olson and Morris Cohen (2) was designed to be suitable for a cooperative and coordinated effort in applied materials research by an interdisciplinary team. The plan and organization of this research forms a paradigm for research consistent with the structure of the KBMR system.

SPECIFICATIONS FOR THE KBMR SYSTEM

The first specification for the system is that it should provide a means of representing, displaying, and interacting with the current research plan. As we have just remarked, it is important to have a detailed plan for the research program. It must be representable as more than a textual statement. It typically describes possible ways of reaching the desired goal, what information must be acquired, and what subgoals must be attained. It may specify sequences of steps designed to move closer toward the target. It may incorporate decisions on the initial procedure as well as tentative decisions on steps to be taken if certain anticipated difficulties are found to block progress. The dynamical interaction of the KBMR with the research plan is especially useful when the plan is complex, when it involves different interrelating phases that may require coordination of work by different researchers, and where the results obtained in one phase will affect the tacit assumptions and even subgoals of other phases.

The KBMR must incorporate an adequate amount of materials knowledge. Materials research identifies understanding of the microstructure as a powerful tool for reasoning about materials properties, and calls for an adequate representation of microstructural features. In the ALADIN system (3-6) features such as grains, grain boundaries, phase descriptions, voids, cracks, etc. are classified and incorporated as schema in a frame representation. In ALADIN, composition, processing, and macroscopic properties are represented by "slots" in the schema. In addition to the many useful features of ALADIN it is further necessary to implement some major modifications of this methodology in order to be able to generalize the representation of processes and models to be most useful for research applications.

Inference methods form an integral part of the KBMR. They involve search through the database, pattern matching, and invocation of models. All knowledge is represented as schemata and there is no distinction between data and rules and no other activity other than creating slots and values. The top level control of the KBMR system is guided by pattern matching. Research plans and procedures have a schema representation. In an interactive session with the KBMR a menu of actions is produced through a pattern matching of the status of the current session and research procedures known to KBMR. If a researcher selects the "NONE OF THE ABOVE" option and enters a new alternative, the KBMR "learns" it and will present it as a menu option at later runs. While the KBMR does not represent experimental procedures or research tools as such, the names of these procedures and tools form pointers to the types of specific information that would be ascertained by these procedures, so that when the results are reported, the KBMR can cue the reporter for this information as well as label the information according to the technique utilized.

ARCHITECTURE OF THE KBMR SYSTEM

The following is a much abridged description of the KBMR architecture, defining briefly the main terms used.

A schema is a named data structure with an arbitrary number of attributes, also called slots, which may be given one or more values. Certain attributes such as IS-A have special significance, and are called relations. Relations

define a network of links between schemata and they make attributes available to related schemata by a mechanism called inheritance. There are other terms such as procedural attachment, which means that a piece of code rather than a value is attached to an attribute. This code is executed every time a value is sought and the result is returned as if it were the value. The reasoning process involves inferring values of attributes in existing or newly created "target" schemata. Acceptable values are first sought through simple retrieval, with or without inheritance. Otherwise, a search is made for the best model. There is a procedure for defining "best". Inferences are themselves represented by schemata, enabling the preservation of knowledge of how a value was obtained as well as the storage of other information used during the inference process. Models may be simple schema or may be attached to pieces of code, also called demons, which can generate values. Models may represent phenomenology or may be deeper, representing details in microstructural processes. Simulation techniques are used to establish consequences of model performance under specified conditions.

SUMMARY OF MAIN FEATURES OF KBMR

Represents research plans for achieving research goals.

Unifies qualitative and quantitative constraints.

Automatically and continuously checks constraints of the design plan.

Has a mixed initiative design process.

Provide knowledge representation for materials information and specifically, information relevant to ultrahigh strength steels.

Represents models of materials, including models relevant to ultrahigh strength steels.

Represents materials processes in terms of models.

Utilizes both qualitative and quantitative models.

Represents experimental results, recording tested variables and models.

Critically compares model predictions with experimental observations.

Interfaces with libraries of numerical codes for performing simulations.

Has tools for viewing and manipulating materials and models databases.

Has tools for performing materials literature searches.

REFERENCES

1. R.J. Harrison, "Artificial Intelligence and Simulation in Materials Science Research," Artificial Intelligence Applications in Materials Science, R.J. Harrison and L.D. Roth, Eds., (Warrendale, PA, Metallurgical Society of AIME, 1987)

2. G.B. Olson and M. Cohen, MIT proposal to National Science Foundation, (1984)

3. M.L. Farinacci, M.S. Fox, I. Hulthage and M.D. Rychener, "ALADIN, a Knowledge-Based System for Alloy Design", Technical Report, Carnegie-Mellon University, Intelligent Systems Laboratory, Robotics Institute, (1986).

4. M.L. Farinacci, M.S. Fox, I. Hulthage and M.D. Rychener, "The development of ALADIN, an Expert System for Aluminum Alloy Design", in Third International Conference on Advanced Information Technology. Gottlieb Duttweiler Institute, Zurich, Switzerland, (Amsterdam, the Netherlands, North-Holland, 1986); Technical Report CMU-RI-TR-86-5, (1986)

5. I. Hulthage, M.D. Rychener, M.S. Fox and M.L. Farinacci, "The use of quantitative databases in ALADIN, an alloy design system", in Coupling Symbolic and Numerical Comuting in Expert Systems, J.S. Kowalik, Ed., (Amsterdam, the Netherlands, North Holland, 1986). Presented at an AAAI Workshop in Bellevue, WA, August, 1985. Technical Report CMU-RI-TR-85-19, (1985)

6. I. Hulthage, M. Przystupa, M.L. Farinacci and M.D. Rychener, "The metallurgical databases of ALADIN", Technical Report, Carnegie Mellon University, Intelligent Systems Laboratory, Robotics Institute, (1986)

Registration List

Ralph P.I. Adler
Chief, Mfg. Engrg. Branch
Army Materials
Technology Laboratory
Arsenal Street
ATTN: SCLMT-MCM
Watertown, MA 02172
(617) 923-5459/AV 955-5459

Iqbal Ahmad
Army Research Office
Materials Division
P.O. Box 12211
Res Triangle Pk, NC 27709

Maurice F. Amateau
Department Head
Engineering Materials Dept.
Pennsylvania State
University
Applied Research Laboratory
P.O. Box 30
State College, PA 16804
(814) 863-4214

Peter M. Anderson
Research Assistant
Cambridge University
Engineering Department
Trumpington Street
Cambridge, ENGLAND CB2 1PZ
011-44-223-332814

Iossif Aslanidis
Ph.D. Student
Massachusetts Institute
of Technology
Building 13-5141
77 Cambridge Avenue
Cambridge, MA 02139
(617) 253-6828

Morris Azrin
Supervisory Metallurgist
Army Materials
Technology Laboratory
405 Arsenal Street
ATTN: SCLMT-MCM
Watertown, MA 02172
(617) 923-5310/AV 955-5310

Joseph M. Barranco
Project Metallurgist
Army Armaments RD&E Center
Benet Laboratories
Watervliet Arsenal
Watervliet, NY 12189-4050
(518) 266-4198/AV 8-974-
4198

Judith Bhansali
Materials Research Engineer
Army Materials
Technology Laboratory
Arsenal Street
ATTN: SCLMT-MCD-P
Watertown, MA 02172
(617) 923-5474/AV 955-5474

Kirit J. Bhansali
Research Metallurgist
Army Materials
Technology Laboratory
Arsenal Street
ATTN: SLCMT-MCM-CSB
Watertown, MA 02172
(617) 923-5212/AV 955-5212

George H. Bishop, Jr.
Director, Mechanical &
Structural Integrity Lab.
Army Materials
Technology Laboratory
405 Arsenal Street
ATTN: SCLMT-MS
Watertown, MA 02172
(617) 923-5742/AV 955-5742

*Affiliation as recorded at time of conference

Gordon A. Bruggeman
Director, Metals & Ceramics
Laboratory
Army Materials
Technology Laboratory
405 Arsenal Street
ATTN: SCLMT
Watertown, MA 02172
(617) 923-5295/AV 955-5295

John H. Bucher
Director, Research &
Quality Control
Lukens Steel Company
Modena Road, ARC C-500
Coatesville, PA 19320
(215) 383-3169

Robert D. Caligiuri
Managing Engineer
Failure Analysis Associates
2225 East Bayshore Road
Palo Alto, CA 94303
(415) 496-7177

Gary M. Carinci
Research Assistant
Massachusetts Institute
of Technology
Room 13-5134
77 Massachusetts Avenue
Cambridge, MA 02139
(617) 253-6923

Raymond A. Cellitti
President
R. C. Associates
122 Columbia
Hinsdale, IL 60521
(312) 323-3651

Richard Chait
Associate Director
Army Materials
Technology Laboratory
Arsenal Street
ATTN: SLCMT-DA
Watertown, MA 02172-0001
(617) 923-5351/5515/AV 955-
5351/5515

Fu-Rong Chen
Postdoctor Associate
Massachusetts Institute
of Technology
Room 13-5122
Cambridge, MA 02139
(617) 253-3321

Morris Cohen
Inst. Professor Emeritus
Massachusetts Institute
of Technology
77 Massachusetts Avenue
Cambridge, MA 02139
(617) 253-3325

Paul J. Cote
Chief, Materials
Engineering Section
Army
Research Branch
Watervliet Arsenal
Watervliet, NY 12189
(518) 266-5481/AV 974-5481

John Cowie
Metallurgist
Army Materials
Technology Laboratory
Arsenal Street
ATTN: SCLMT-MCM
Watertown, MA 02172
(617) 923-5206/AV 955-5206

Joseph R. Crisci
Assistant Department Head
Research
David Taylor Naval Ship
R&D Center
Building 3A
Annapolis, MD 21402
(301) 267-2462

Craig V. Darragh
Manager, Application
Development - Steel
Timken Company
1835 Dueber Avenue SW
Canton, OH 44706
(216) 438-3236

Mark Eberhart
Scientist
Los Alamos National
Laboratory
G 730
Los Alamos, NM 87545
(505) 667-0022

William T. Ebihara
Chief, Armaments Technology
Division
Army Armaments RD&E Center
Building 355
ATTN: SMCAR-AET
Picatinny Ars NJ 07806-5000
(201) 724-2326/AV 880-2326

Norman A. Fleck
Lecturer
Engineering Department
Cambridge University
University Engrg. Dept.
Cambridge, ENGLAND CB2 1PZ
223-332650

S. Floreen
Principal Engineer
Knolls Atomic Power
Laboratory
P.O. Box 1072
Schenectady, NY 12301
(518) 395-6093

Paul Fopiano
Army Materials
Technology Laboratory
405 Arsenal Street
ATTN: SLCMT
Watertown, MA 02172
(617) 923-5327/AV 955-5327

Rosendo Fuquen
Manager, Material Sciences
Timken Company
1835 Dueber Avenue
Canton, OH 44706
(216) 497-2233

Roger A. Gagne
Acting Chief, Processing
Technology Division
Army Material
Technology Laboratory
Arsenal Street
ATTN: SCLMT-MCD-P
Watertown, MA 02172
(617) 923-5579/AV 955-5579

Anthony J. Garratt-Reed
Principal Res. Scientist
Massachusetts Institute
of Technology
Room 13-1027
77 Massachusetts Avenue
Cambridge, MA 02139
(617) 253-4622

Warren M. Garrison, Jr.
Associate Professor
Carnegie Mellon University
Pittsburgh, PA 15215

Alan J. Goldman
Chief, Armor Materials
Development Branch
Army Materials
Technology Laboratory
ATTN: SLCMT-MCP-M
Watertown, MA 02172
(617) 923-5063/AV 955-5063

Mark J. Gore
Massachusetts Institute
of Technology
77 Massachusetts Avenue
Cambridge, MA 02139
(617) 253-6923

Mica Grujicic
Research Scientist
Massachusetts Institute
of Technology
Room 13-5014
Cambridge, MA 02139

Gregory N. Haidemenopoulos
Massachusetts Institute
of Technology
Room 13-5001
77 Massachusetts Avenue
Cambridge, MA 02139

Ralph J. Harrison
Research Physicist
Army Materials
Technology Laboratory
Arsenal Street
ATTN: SCLMT-MSR-MM
Watertown, MA 02172
(617) 923-5050/AV 955-5050

Ray Hawkins
Section Head
Ministry of Defence (PE)
RARDE
Fort Halstead
Sevenoaks, Kent
ENGLAND TN14 7BP
959 32222

Clive Hayzelden
Assistant Professor
Harvard University
Gordon McKay Laboratory
9 Oxford Street
Cambridge, MA 02138
(617) 495-9525

Erhard Hornbogen
Professor, Material Science
Ruhr-Universitat Bochum
Universitatsstrasse 150
Postfach 102148
4630 Bochum 1
FEDERAL REPUBLIC OF GERMANY
0234-700-3022

John W. Hutchinson
Professor of Mechanics
Harvard University
Div. of Applied Sciences
29 Oxford Street
Cambridge, MA 02138
(617) 495-2848

Richard M. Ingersoll
Engineering Supervisor
General Dynamics Land
Systems
1902 Northwood
Troy, MI 48084
(313) 362-8212

Behram M. Kapadia
Assoc. Research Consultant
U.S.S. Technical Center
4000 Tech Center Drive
Monroeville, PA 15146
(412) 825-2296

Joseph A. Kapp
Materials Research Engineer
Army Armaments
RD&E Center
Materials Engineering
Section
Watervliet, NY 12189-4050
(518) 266-5124/AV 955-5124

Genrich Krasko
Massachusetts Institute
of Technology
77 Massachusetts Avenue
Cambridge, MA 02139

George Krauss
AMAX Foundation Professor
Metallurgical & Materials
Engineering Department
Colorado School of Mines
Golden, CO 80401
(303) 273-3770

Eric B. Kula
Chief, Metals Research Div.
Army Materials
Technology Laboratory
405 Arsenal Street
ATTN: SCLMT-MCM
Watertown, MA 02172
(617) 923-5469/AV 955-5469

Hyuck Mo Lee
Graduate Student
Massachusetts Institute
of Technology
Building 13-5130
77 Massachusetts Avenue
Cambridge, MA 02139
(617) 253-6822

Alan J. Levy
Assistant Professor
Syracuse University
Dept. of Mechanical
& Aerospace Engineering
139 Link Hall
Syracuse, NY 13210
(617) 923-5268

Gerald T. Looby
Manager, Special Metals
Technical Service
LTV Steel
Special Metals Division
2201 Harrison Avenue SW
Canton, OH 44706
(216) 438-5766

James Maloney
Senior Research Engineer
Latrobe Steel Company
2626 S. Ligonier
Latrobe, PA 15650
(412) 537-6407

C. J. McMahon, Jr.
Dept. of Material Science
& Engineering
University of Pennsylvania
Philadelphia, PA 19104-
6272

Lawrence V. Meisel
Physicist
Army Armaments RD&E Center
Benet Laboratories
Broadway
Watervliet, NY 12189
(518) 266-5016

John Mescall
Research Mathematician
Army Materials
Technology Laboratory
405 Arsenal Street
ATTN: SCLMT-MSR
Watertown, MA 02172
(617) 923-5442/AV 955-5442

Harold Mindlin
Program Manager
Battelle-Columbus Division
505 King Avenue
Columbus, OH 43212
(614) 424-4425

Terry Mohr
Director, Research
Timken Company
1835 Dueber Avenue
Canton, OH 44706
(216) 497-2018

Jonathan S. Montgomery
Materials Engineer
Army Materials
Technology Laboratory
405 Arsenal Street
ATTN: SCLMT
Watertown, MA 02172
(617) 923-5133/AV 955-5133

Michael J. Morgan
Research Metallurgist
DuPont (E.I.) De Nemours
Savannah River Laboratory
Aiken, SC 29801
(803) 725-2245

Tapan Mukherjee
Program Director
National Science Foundation
Room 1130
1800 G Street N.W.
Washington DC 20550
(202) 357-7710/FTS 8-202-
357-7710

Marjorie Natishan
Materials Engineer
David Taylor Naval Ship
R&D Center
Annapolis, MD 21402
(301) 267-2368/AV 281-2368

Alan Needleman
Professor
Brown University
Box D
Providence, RI 02912
(401) 863-2863

Gregory B. Olson
Senior Research Associate
Massachusetts Institute
of Technology
Building 13-5050
77 Massachusetts Avenue
Cambridge, MA 02139
(617) 253-6901/923-5212

Neil Paton
Director, Materials Engrg.
& Technology
Rocketdyne Division
Rockwell International
Corporation
6633 Canoga Avenue
Canoga Park, CA 91304

Harry C. Rogers
Head
Materials Engineering
Drexel University
32nd & Chestnut Street
Philadelphia, PA 19104
(215) 895-2322/2323

Jungsuk Ryu
Metallurgical Engineer
General Electric Company
100 Plastics Avenue
Pittsfield, MA 01201
(413) 393-2940

Michael L. Schmidt
Senior Metallurgist
Tool & Alloy R&D
Carpenter Technology Corp.
P.O. Box 14662
Reading, PA 19612-4662
(215) 371-2792

Wilbur C. Simmons
Chief, Materials
Science Branch
U.S. Army Research Office
RD & S Gp (UK)
Box 65
FPO NY 09510
ENGLAND
01-409-4423

George D. W. Smith
University Lecturer
Department of Metallurgy
Oxford University
Parks Road
Oxford
ENGLAND OX1 3PH
865-273762

Gilbert R. Speich
Professor & Chairman
Department of Metallurgical
& Materials Engineering
Illinois Institute of
Technology
IIT Center
Chicago, IL 60616
(312) 567-3050

Michael F. Stevens
Section Leader
Los Alamos National
Laboratory
MS G730
Los Alamos, NM 87545
(505) 667-4414

Keith Taylor
Engineer
Bethlehem Steel Corp.
Research Department
Bethlehem, PA 18016
(215) 694-6747

Timothy S. Thomas
Materials Engineer
U.S. Secret Service
1310 L Street NW, Rm 800
Washington, DC 20005
(202) 566-8294

Dennis Tracey
Chief, Mechanics of
Materials Branch
Army Materials
Technology Laboratory
Arsenal Street
ATTN: SCLMT-MSR-MM
Watertown, MA 02172
(617) 923-5356/AV 955-5356

Floyd R. Tuler
Professor
Worcester Polytechnic Inst.
100 Institute Road
Worcester, MA 01609
(617) 793-5299

Diane M. Vanderwalker
Electron Microscopist
Army Materials
Technology Laboratory
Arsenal Street
ATTN: SCLMT-OMM
Watertown, MA 02172
(617) 923-5358/AV 955-5358

Richard H. Wagner
Head, Material Science &
Engineering Department
GKSS Research Center
Max-Planck-Str. 1
D 2054 Geesthacht
FEDERAL REPUBLIC OF GERMANY

Jian Sheng Wang
Research Associate
Harvard University
Div. of Applied Sciences
29 Oxford Street
Pierce Hall, Rm 285
Cambridge, MA 02138
(617) 495-8245

John F. Watton
Postdoctoral Res. Associate
Massachusetts Institute
of Technology
Room 13-5138
77 Massachusetts Avenue
Cambridge, MA 02139
(617) 253-6920

Volker Weiss
Professor, Engrg. & Physics
Syracuse University
409 Link Hall
Syracuse, NY 13244-1240
(315) 423-3918

Edward S. Wright
Director
Army Materials
Technology Laboratory
405 Arsenal Street
ATTN: SCLMT-D
Watertown, MA 02172
(617) 923-5275/AV 955-5275

Victor F. Zackay
President
Materials & Methods, Inc.
1014 West Road
New Canaan, CT 06840
(203) 966-7704

Anthone Zarkades
Metallurgist
Army Materials
Technology Laboratory
Arsenal Street
ATTN: SCLMT-MCP-M
Watertown, MA 02172
(617) 923-5067/AV 955-5067

Index

INDEX

NOTE: The following index of key words is page numbered according to the first page of the paper.

U

V

W

Z